Texas A&M University

Mechanical Engineering Department

Turbomachinery Laboratory

ROTORDYNAMIC PERFORMANCE OF A ROTOR SUPPORTED ON GAS FOIL BEARINGS

Research Progress Report to the Turbomachinery Laboratory

TRC-B&C-2-05

by

Dario Rubio

Research Assistant

Luis San Andrés

Principal Investigator

May 2005

ROTORDYNAMIC PERFORMANCE OF A ROTOR
SUPPORTED ON GAS FOIL BEARINGS"

EXECUTIVE SUMMARY

Foil gas bearings appear to satisfy most requirements for oil-free turbomachinery, i.e. relatively simple in construction, ensuring low drag friction and reliable high speed operation. However, gas foil bearings have a limited load capacity and minimal amounts of damping. A test rig for the rotordynamic evaluation of gas foil bearings was constructed. A DC router motor, 25 krpm max speed, drives a 2.2 lb hollow rotor supported on two bump-type foil gas bearings ($L=D=1.5$"). Measurements of the test rotor dynamic response were conducted for increasing mass imbalance conditions. Typical waterfalls of rotor coast down response from 25 krpm to rest evidence the onset and disappearance of severe subsynchronous motions with whirl frequencies at ~ 50% of rotor speed, roughly coinciding with the (rigid mode) natural frequencies of the rotor-bearing system. The amplitudes of motion, synch and subsynchronous, increase (non) linearly with respect to the imbalance displacement. The rotor motions are rather large; yet, the foil bearings, by virtue of their inherent flexibility, prevented the catastrophic failure of the test rotor. Tests at the top shaft speed, 25 krpm, did not excite subsynchronous motions; the unstable zone being well confined (12 to 22 krpm). Surprisingly enough, external air pressurization on one side of the foil bearings acted to reduce the amplitudes of motion while the rotor crossed its critical speeds and ameliorated the severity of the subsynchronous vibrations. An air-film hovering effect may enhance the sliding of the bumps thus increasing the bearings damping action. While coasting down, the rotor speed decreased rather rapidly, thus denoting a significant rotational drag due to operation with minute film gaps. Post-test inspection of the rotor evidenced sustained wear at the locations in contact with the bearings' axial sides. However, the foil bearings are almost in pristine condition, except for transfer of shaft coating material to the top foils.

LIST OF CONTENTS

LIST OF FIGURES

7

LIST OF TABLES

NOMENCLATURE

c	Estimated foil bearing radial clearance
c_{nom}	Nominal foil bearing radial clearance
E	Bump modulus of elasticity
g	Initial air gap
ID	Inner diameter of FB
K_F, K_W	Free ends and free end -fixed end bump stiffness
L	Axial bearing length
M, M_B	Rotor mass and bearing mass
m	Imbalance mass
N_B	Number of bumps
OD	Outer FB diameter
P_a	Ambient pressure, 1.01 bar
p	Bump pitch
r_e	Radius for insertion of imbalance mass
S	Shim thickness
t_f	Foil thickness
u	Imbalance displacement
w	$w = \dfrac{W_n}{P_a \cdot L \cdot D}$, Load coefficient
X, Y	Horizontal and vertical rotor displacements
δ_S	Rotor displacement due to shim insertion
δ_{static}	Resulting bearing static deflection due to fraction of rotor weight supported
ϕ	Angle of imbalance mass insertion
κ	$\kappa = \dfrac{K}{E(T) \cdot t}$. FB dimensionless stiffness coefficient
Λ	$\Lambda = \dfrac{6\mu\Omega}{P_a}\left(\dfrac{R}{C}\right)^2$. Bearing speed number

Subscript

DE	Drive end
FE	Free end

I. INTRODUCTION

High performance oil-free turbomachinery implements gas foil bearings *(FBs)* to improve mechanical efficiency in compact units. *FBs* fulfill most of the requirements of novel oil-free turbomachinery by increasing tenfold their reliability in comparison to rolling elements bearings, for example [1]. Foil bearings are made of one or more compliant surfaces of corrugated metal and one or more layers of top foil surfaces. The compliant surface, providing structural stiffness, comes in several configurations such as bump-type (see Figure 1), leaf-type and tape-type, among others. *FB*s operate with nominal film thicknesses larger than those found in a geometrically identical rigid surface bearing, for example, since the hydrodynamic film pressure generated by rotor spinning "pushes" the *FB* compliant surface [2, 3].

*FB*s enable high speed operation and large load capacity, in particular in third generation configurations [4] the underlying compliant structure provides a tunable structural stiffness [5 - 8]. In gas *FB*s, Coulomb type damping arises due to the relative motion between the bumps and the top foil, and between the bumps and the bearing support wall [9, 10].
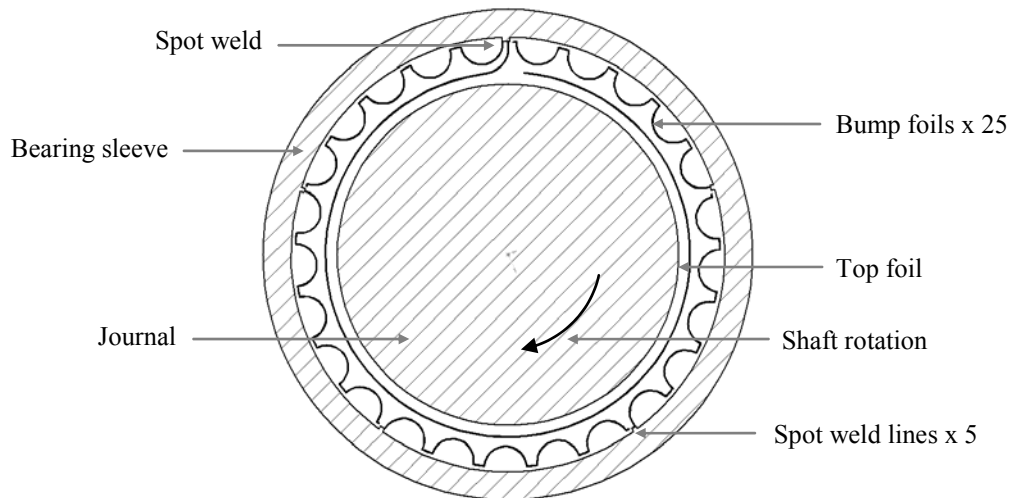
Figure 1 Schematic representation of a bump-type gas foil bearing

In bump-type foil bearings, the top foil supported by compliant bumps, deforms elastically under the pressure field created by the hydrodynamic film. The bearing stiffness combines that resulting from the deflection of the bumps and also by the hydrodynamic film generated when the shaft rotates. Damping arises due to the relative motion between the bumps and the top foil or between the bumps and the bearing wall, i.e. Coulomb type damping [5]. The foil bearing design constrains the direction of shaft rotation to only one direction. Due to the hydrodynamic film created by rotor spinning, the top foil expands resulting in a larger film thickness than in a rigid

bearing, for example. At start up, the back of the foil is in contact with the bump foils and the outer side of the foil is in contact with the journal. As the rotor spins to a sufficiently high speed (i.e. when lift off occurs), the top foil contracts as air is dragged into a thin annular film between the foil and the shaft.

Gas foil bearings have been applied successfully to a wide range of high-speed rotating machinery such as air cycle machines (ACMs), auxiliary power units (APUs), and cryogenic turbocompressors, among others [11]. Field experience with foil bearing commenced in the mid 60's by introducing the first production air cycle machines (ACM) using foil gas bearings [1]. The air cycle machines are the heart of the environmental control system (ECM) used in aircraft to control cooling, heating and pressurization of aircraft. These units, developed for the DC-10 ECM, proved to be far more reliable than previous ball bearing units. Further research and experimentations continued in the 70's to increase load capacity and damping capability. Based on the successful performance, ACMs for other aircraft such as in the EMB-120, ATR-42 and Boeing 767/757, started to implement foil gas bearings. For instance, the foil bearing air cycle machine on the 747 aircraft demonstrated a mean time between failures (MTBF) in excess of 100,000 hours. Recently, the latest ECS system for the Boeing aircraft 777 uses a four-wheel foil gas bearing ACM. This unit has passed 36,000 start-stop cycles, which is equivalent to 30 years life of the machine.

For over three decades foil bearings have been successfully applied in ACMs used for aircraft cabin pressurization. These turbomachines utilize "Generation I" foil air bearings along with conventional polymer solid lubricant [12]. Based on the technical and commercial success of ACMs; oil-free technology moves into gas turbine engines. The first commercially available Oil-free gas turbine was the 30 kW Capstone microturbine conceived as a power plant for hybrid turbine electric automotive propulsion system [12]. This microturbine utilizes patented foil gas bearings categorized as "Generation III" bearings. In addition, future applications of oil-free turbomachinery using foil bearing include large Regional Jet engines and supersonic Business Jet engines. For these applications, the system benefits include, among others, weight and maintenance reduction.

Remarkable improvements in high temperature limits are obtained by using coatings (solid lubricants). Process gases can operate at very high temperatures without chemically breaking down as opposed to conventional lubricant oils. In addition, oil lubricants lead to larger power

losses due to friction at the interface between the fluid and bearing shell. Having established good reliability records in many high-speed turbomachinery at extreme temperatures, *FBs* show great credentials to replace ball bearings in cryogenic fluid turbomachinery [13]. Applications of gas foil bearing in process fluid turbocompressors have been also noted in the open literature. Chen et al. [14] present an application example of the successful replacement of a tape-type foil bearing for a bump-type foil bearing in a helium turbocompressor. Both bearing types are described, as are the steps involved in the design and fabrication of the bump bearing, and results of a comparison test between the original and replacement bearings. Methods to analyze bump-type foil bearing with commercially available software are reviewed to further emphasize the inherent simplicity of *FBs*. The frictional torque of foil bearings is greater when the rotor starts up and decreases when the rotor speed is high enough to generate a hydrodynamic film. The same characteristic is observed from the coastdown response of the rotor. Steady state and speed transient tests show that the implementation of the bump-type foil bearing increased the critical speed of the original system because the bearing stiffness is likely to be greater than that of the previous design (tape-type foil bearings).

Despite the level of progress advanced in recent years, foil bearing design is still largely empirical due to its mechanical complexity. As part of the current research on gas foil bearing at Texas A&M University, this report provides an experimental investigation of the rotordynamic performance of a light rotor supported on two bump-type gas foil bearings. The results serve as benchmark for calibration of analytical tools under development at TAMU.

II. LITERATURE REVIEW ON GAS FOIL BEARINGS STRUCTURAL PARAMETERS AND ROTORDYNAMIC PERFORMANCE

An extensive part of the literature on foil gas bearings relates to their structural characteristics, namely structural stiffness, dry friction coefficient and equivalent viscous damping. The compliant structural elements in *FB*s constitute the most significant aspect on their design process. With proper selection of foil and bump materials and geometrical parameters, the desired stiffness, damping and friction forces can be achieved. Ku and Heshmat [5] first developed a theoretical model of the corrugated foil strip deformation used in foil bearings. The model introduces local interaction forces, the friction force between the bump foils and the bearing housing or top foil, and the effect of bump geometry on the foil strip compliance. Theoretical results under constant and variable (triangular) load distribution profiles indicate that bumps located at the fixed end of a foil strip provide higher stiffness than those located at its free end. Higher friction coefficients tend to increase bump stiffness and may lock-up bumps near the fixed end. Similarly, the bump thickness has a small effect on the local bump stiffness, but reducing the bump pitch or height significantly increases the local bump stiffness.

In a follow-up paper, Ku and Heshmat [6] present an experimental procedure to investigate the foil strip deflection under static loads. Identified bump stiffnesses in terms of bump geometrical parameters and friction coefficients corroborate the theoretical results presented in [5]. Through an optical track system, bump deflection images are captured indicating that the horizontal deflection of the segment between bumps is negligible compared to the transversal deflection of the bumps. The identification of bump strip stiffness, from the load-versus-deflection curves, indicates that the existence of friction forces between the sliding surfaces causes the local stiffness to be dependant on the applied load and ensuing deformation.

Rubio and San Andrés [8] further develop the structural stiffness dependency on applied load and displacement. An experimental and analytical procedure aims to identify the structural stiffness for an entire bump-type foil bearing. A simple static loader set up allows observing the *FB* deflections under various static loads. Three shafts of increasing diameter induce a degree of preload into the *FB* structure. Static measurements show nonlinear *FB* deflections, varying with the orientation of the load relative to the foil spot weld. Loading and unloading tests evidence hysteresis. The *FB* structural stiffness increases as the bumps-foil radial deflection increases (hardening effect). The assembly preload results in notable stiffness changes, in particular for

small loads. A simple analytical model assembles individual bump stiffnesses and renders predictions for the *FB* structural stiffness as a function of the bump geometry and material, dry-friction coefficient, load orientation, clearance and preload. The model predicts well the test data, including the hardening effect. The uncertainty in the actual clearance (gap) upon assembly of a shaft into a *FB* affects most the predictions.

Similarly, Ku [15] describes an experimental investigation to characterize the structural dynamic force coefficients of corrugated bumps used in foil bearings. Dynamic force perturbations are imposed to a six-bump strip under different test conditions and various bump geometrical configurations. Test results show that dynamic structural stiffnesses decrease with the amplitude of motion and increase with the static load. The friction coefficient for various surface coatings are determined empirically by matching the values of the dynamic structural stiffness with analytical predictions developed in [5]. The dynamic structural stiffness best correlates with theoretical values when selecting dry friction coefficients ranging from 0.4 to 0.6, depending on the surface coating.

The structural damping mechanism in foil bearings is well known. Various investigations have focused into this *FB* structural characteristic. Heshmat and Ku [16] develop an experimental procedure to identify the structural stiffness and equivalent viscous damping coefficient by exciting, with two electromagnetic shakers, a non-rotating shaft supported on *FB*s. Structural dynamic coefficients, determined from a force equilibrium on the *FB* housing, indicate that the direct stiffness and equivalent viscous damping decrease with increasing dynamic load amplitudes. In addition, an increase in the excitation frequency decreases the direct viscous damping and increases the direct stiffness. An analytical model, advanced in [9, 10], accounting for the bumps curvature effect, force interaction between bumps, and dry friction coefficient under sliding conditions, provides predictions of dynamic force coefficients in foil bearings. The analytical model in [9] determines dynamic structural stiffness based on the perturbation motion of the journal center with respect to its static equilibrium position. Equivalent viscous damping coefficients are extracted from the hysteresis loop area enclosed by the journal center locus undergoing dynamic motions. Dynamic force coefficients are found to be in agreement with experimental results using a constant dry friction coefficient ranging from 0.4 to 0.6 for the model predictions. Also, the identified dynamic force coefficients are anisotropic and highly non linear with respect to the amplitude of displacement perturbation.

Recently, Salehi et. al [17] perform dynamic forced tests on corrugated metal sheets (bump foil strips) affixed within an arcuate surface. Dynamic force excitations are exerted on the bump strip using an electromagnetic shaker at various load and frequency conditions. Equivalent viscous damping coefficients and dry friction forces are extracted from the resulting hysteresis loops (force versus displacement) for various test conditions. In addition, bump foil stiffness and viscous damping coefficients are identified from the complex mechanical impedance formulation using a single degree of freedom model. Experimental results of dynamic force coefficients for the bump strips are used to develop a parametric (dimensionless) relationship between frictional damping and test conditions of load (W), amplitude of motion (X) and frequency (f). Based on experimental results, the parametric relationship of viscous damping is found to decrease with increasing frequencies, $C_{EQ} \propto 1/f$, and amplitude of motions, $C_{EQ} \propto 1/X$, while increasing with the magnitude of dynamic load, $C_{EQ} \propto W$. In terms of dry friction coefficients (μ), a parametric relationship is also found based on the experimental results. Experimental results of dry friction coefficients render values ranging from 0.1 to 0.4 for increasing excitation frequencies from ~ 0 Hz to ~ 600 Hz.

The literature concerned with the rotordynamic characteristics of foil bearings is quite limited. The results achieved in previous works represent important background for the current research project. Table 1 summarizes the major findings in experimental investigations of foil bearing rotordynamic performance.

Table 1 List of references on experimental investigations on *FB* rotordynamic performance and major findings

Authors	Test Apparatus	Type of Rotordynamic Experiments	Observations
1994 Heshmat, H. *Ref (18)*	Rotor (1.52 kg) supported on foil journal bearings and driven by an integral impulse-type air turbine.	Coastdown tests from 132,000 rpm above first two rigid body mode frequencies.	Major frequencies are subsynchronous vibrations associated to rotor rigid body frequencies (cylindrical and conical). Increasing *FB* eccentricity displacements, larger than the nominal clearance, lead to significant enhancements on load capacity.
2000 Heshmat, H. *Ref (19)*	Flexible rotor (3.9 kg) supported on foil journal bearings	Coastdown tests from 45,000 rpm above first two rigid body mode frequencies and first bending mode.	No subsynchronous vibrations experienced until reaching the bending critical speed where rigid body frequencies dominated rotor response.
2001 Howard, S., et. al *Ref (20)*	N/A	Steady state tests at 30,000 rpm. Applied bearing load varies from 11 to 89 N and temperature ranges from 25° to 538°C	Steady-state stiffness does not vary with temperature until the temperature reaches ~538°C where stiffness drops due to foil material's loss of strength. Effect of temperature on stiffness is larger at high loads than at low loads. No subsynchronous vibrations acknowledged.
2002 Walton, J., and Heshmat, H. *Ref (21)*	Air cycle machine simulator supported on "third generation" foil journal bearings.	Coastdown tests from 61,000 rpm	Steady state motions at subsynchronous rigid body mode frequencies limited in magnitude. Similar dynamic performance of the rotor system for vertical and horizontal operations.
2002 Swason E., et al. *Ref (22)*	Rotor (54.5 kg) supported on active magnetic bearings and compliant foil bearings.	Coastdown tests from 16,000 rpm with foil bearing alone.	Heaviest shaft to be supported on foil bearings. Steady state vibrations at subsynchronous rigid body mode frequencies small in magnitude.
2003 Lee, Y.B., et. al *Ref (23)*	Two-stage centrifugal compressor supported on conventional bump foil journal bearing and viscoelastic foil journal bearing	Steady state tests at compressor operating speed 32,000 rpm	Used first generation *FB*s, subsynchronous vibrations associated with rigid mode frequencies of the shaft prevailed over the synchronous motions. Using viscoelastic layer *FB*s, subsynchronous motions are reduced.
2004 Hou, Y., et. al *Ref (24)*	Rotor supported on two foil journal bearing with elastic support	Run-up tests to 151,000 rpm	Subsynchronous vibrations are small compared to synchronous component throughout the whole operating region.

17

Heshmat [18] performed high-speed tests using a journal foil bearing to establish the rotor-bearing stability characteristics and speed performance. Increasing load conditions and large unbalance magnitudes were applied to the test rotor. The rotating system did not evidence harmful synchronous amplitudes due to the increase in the residual unbalance throughout the entire speed range (up to 132,000 rpm). On the other hand, load capacity tests consisted of applying a load to a center bearing at an arbitrary speed until a high-speed rub between the mating surfaces of the shaft and foil occurred. Unlike rigid wall bearings, the foil air bearings exhibited eccentricity displacements (e) larger than their nominal clearance due to the compliance of the bump foils. Precisely, these larger eccentricity displacements lead to significant enhancements on the load capacity coefficient (w)[1]. In general, the load capacity coefficients (w) and eccentricity displacements (e) present little variance at low values of bearing speed parameter $(\Lambda < 1.5)$[2]. After that point, w and e rise at a steep rate with an increase in Λ. Experimental data collected from the rotor/bearings system shows relatively large subsynchronous vibration components in comparison to the synchronous component. However, the rotating system reached a limit cycle amplitude and operated safely for a large period of time.

Heshmat [19] also investigates the foil bearing performance in a test rotor operating above its bending critical speed. Free-free rap test on the long test rotor allows identifying the bending natural frequencies and corresponding nodes of the test rotor. Based on the bending-mode nodes, three different locations for the foil bearing pedestal are examined to determine an optimum position for operations above the rotor bending critical speed. Locating the bearing pedestals at the furthest position from the mode nodes allows super bending critical operations of the rotor/bearing system (2.5 times the first bending critical speed). Operation beyond the first bending critical speed presents small synchronous vibration amplitudes throughout entire speed range. However, large subsynchronous components are observed, at the first rigid body mode and its harmonics, when crossing the first bending critical speed. The subsynchronous components reached limit cycle amplitude typical of dry friction damped systems.

---

[1] Load capacity coefficient defined as $w = \dfrac{W_n}{P_a \cdot L \cdot D}$, where W_n is bearing load, P_a is ambient pressure, L and D are bearing length and diameter, respectively.

[2] Bearing speed parameter defined as $\Lambda = \dfrac{6\mu\Omega}{P_a}\left(\dfrac{R}{C}\right)^2$, where μ is gas viscosity, Ω is rotor speed, R is bearing radius, and C is radial clearance.

DellaCorte and Valco [25] introduce a simple "rule of thumb" method to estimate the load capacity in foil gas journal bearings. The method relates the bearing load capacity to the bearing size and the speed through an empirically based load capacity coefficient, D. Based on previous experiments; DellaCorte and Valco determine that the load capacity is a linear function of the surface velocity and bearing projected area. Three generations of foil bearings are selected to validate this method. First generation foil bearings developed in the 70's reach a load capacity coefficient of $D = 0.4$. However, latest foil bearing designs have an improved load capacity with a D coefficient up to 1.4.

A comprehensive analytical model of the foil bearing rotordynamic performance is essential to reproduce experimental investigations and to assure a proper design and implementation of foil gas bearings in novel turbomachinery applications. Peng and Carpino [26] develop a finite difference formulation, coupling hydrodynamic and elastic foundation effects, to calculate stiffness and damping force coefficients in foil bearings. The model is simply described as impedances in series representing the structural and hydrodynamic support forces. The results from the analytical procedure show that the bearing direct stiffness increases with rotor speed and generally decreases with increased bump compliance. At low rotor speeds, the compliance of the bearing depends primarily on the gas film, which is relatively soft compared to the stiffness of the elastic foundation. In contrast, at high speed operations, the stiffness of the gas film is large compared to the stiffness of the foundation and the compliance of the bearing depends primarily on its elastic foundation. Although these results do not include damping resulting from Coulomb friction, the dynamic force coefficients are significantly reduced due to the elastic foundation in comparison to plain journal bearing coefficients.

San Andrés [27] presents a coupled turbulent bulk-flow and simple structural analysis of a three pad foil bearing for cryogenic fluid applications. The foil structure model consists of a complex structural stiffness with a loss factor, η, denoting hysterical damping, whereas the fluid film contribution is assessed using an isothermal analysis for turbulent bulk-flow of variable liquid properties. The calculated foil bearing force coefficients, namely "viscous" damping and stiffness, show a strong dependency with excitation frequency. The loss factor, η, reduces the direct stiffness coefficients and increases the cross coupled stiffness. A strong effect of the dry friction on the "viscous" damping coefficients at low frequencies is evident while at high frequencies the effect of structural damping is less significant.

As the potential use of foil bearings in novel turbomachinery applications, the need of higher *FB* load capacities and enhancements in the *FB* damping capability are crucial. Lee et al. [28, 29] introduce a viscoelastic material to enhance the damping capacity of foil bearings. The rotordynamic characteristics of a conventional foil bearing and a viscoelastic foil bearing are compared in a rotor operating beyond the bending-critical speed. Experimental results for the vibration orbit amplitudes show a considerably reduction at the critical speed by using the viscoelastic foil bearing. Furthermore, the increased damping capability due to the viscoelasticity allows the suppression of nonsynchronous motion for operation beyond the bending critical speed. In term of structural dynamic stiffness, the viscoelastic foil bearings provide similar dynamic stiffness magnitudes in comparison to the conventional foil bearings.

Foil gas bearings require solid lubrication (coatings) to prevent wear and reduce friction at start-up and shut-down prior to the development of the hydrodynamic gas film. Earlier investigations have revealed that with proper selection of solid lubricants the bearing rotordynamic performance can be significantly improved. DellaCorte et al. [30] present an experimental procedure to evaluate the effects of solid lubricants applied to the shaft and top foil surface on the load capacity of a generation III foil gas bearing. The temperature conditions for the load capacity tests ranged from 25°C to 650°C. A baseline coating of PS304 is plasma sprayed to the test shaft while various foil coatings, such as cured polyimide and chatodic arc aluminum bronze, aim to improve friction and wear properties. The PS304 coating is a plasma spray composite made from a power blend of NiCr, Cr_2O_3, Ag, BaF_2/CaF_2. Each constituent in the PS304 performs a unique function; see reference [30] for details. Sacrificial solid lubricants (polyimide, MoS_2), are overcoated to the PS304 shaft coatings in order to provide low friction during low temperature operations while at high temperature they burn away leaving the PS304 as the primary coating. Experimental results show that the best bearing performance (maximum load capacity) is achieved when the foil and the shaft have good solid film lubricant characteristics. The presence of the non-galling PS304 coating on the shaft and Al-Cu on the top foil also enhances the bearing performance. Based on the test results, the best performance upon installation is achieved using an effective sacrificial solid lubricant film such as MoS_2.

FB rotordynamic performance can be also compromised by the selection of the bearing preload. For instance, foil bearings with large preloads are susceptible to excessive thermal effects and high lift-off torques. Whereas *FB*s subjected to small preloads exhibit a decrease in

load capacity coefficients [20]. Radil et al. [31] study the effect of radial clearance on the *FB* performance. The authors follow an empirical procedure to estimate the linear region of *FB* structural deflection, and define this overall displacement as the *FB* clearance. This ad-hoc practice does not necessarily provide the actual foil bearing clearance since the *FB* structural deflection is highly nonlinear with respect to the applied static load. In the same paper the authors evaluate the influence of radial clearance on the bearing load capacity coefficient. Two foil bearings are tested at different initial radial clearances, below and above the nominal radial clearance (obtained experimentally). Modification to the radial clearance is accomplished by incrementally reducing the outside diameter of the mating journal using an in-place grinding. The experimental results evidence a strong effect of radial clearance on the foil bearing load capacity coefficients. Both foil bearings exhibit an optimum radial clearance that produced a maximum load capacity coefficient. Based on the experimental results of load capacity versus radial clearance, the authors conclude that relative to the optimum clearance (maximum load capacity) there are two distinct regimes, i.e. heavily and lightly preloaded zones.

To date there are no archival publications showing the experimental identification of the complete set of rotordynamic coefficients in a gas foil bearing. Only, Howard et. al [20] forward an experimental procedure to identify steady state direct stiffness in *FB*s operating at elevated temperatures. Cross-coupled stiffness coefficients were not identified in this experimental procedure. The experiments consisted of running the *FB* at constant speed while applying a constant load. Steady-state stiffness coefficients (κ)[3] are found to increase with the applied load and to decrease with shaft speed. Also, steady-state stiffness does not vary with temperature until reaching ~538 ºC, where the stiffness drops due to the foil material loss of mechanical strength.

Howard et. al [32] characterize *FB* dynamic stiffness and damping at various temperature, loads and speed conditions from impact excitations exerted to a test *FB*. A two-degree of freedom system models the ensuing *FB* transient response and compares experimental data to both exponential (viscous damping) and linear (Coulomb damping) decay trends. The method provides a better understanding of the dominating energy dissipation mechanism for all test regions. The identified dynamic stiffness varies as much as 200% with large changes in load and

---

[3] Dimensionless FB stiffness coefficient defined as, $\kappa = \dfrac{K}{E(T) \cdot t}$, where K is the dimensional stiffness, E is the young modulus of the foil material, T is the temperature and t is the foil thickness.

speed. Experimental results also indicate that at high temperatures and low active loads, the gas film is soft compared to the foil structure, i.e. viscous damping behavior. Conversely, for high loads and low temperatures, the bearing behaves like a dry friction damped system with the gas film being stiffer than the foil structure.

III. DESCRIPTION OF TEST FOIL BEARINGS AND EXPERIMENTAL ROTOR/BEARING FACILITY

This section describes the test foil bearings and the experimental facility used in the rotordynamic tests. A detailed overview of the main dimensions and material properties of the test foil bearings are presented as well as the nominal imbalance condition of the test rotor.

III.1. DESCRIPTION OF TEST FOIL BEARINGS

Figure 1 shows a schematic view of a bump-type foil bearing support. The test bump-type foil bearing configuration consists of four bump strips, each with five bumps, aligned axially. The end of a strip is welded to the bearing sleeve while the other end is free. A total of five bump strips are placed around the bearing sleeve, each of them welded at one end and free at the other. The test foil bearings have a total of twenty five bumps around the bearing sleeve. The top foil, coated with Teflon of thickness 25.4 μm, consists of a thin metal sheet welded at the bearing sleeve at one end (spot weld) and free at the other end.

The test foil bearing design corresponds to a "second generation" foil bearing with stiffness characteristics of the foil structure varying either axially along the bearing length or in the circumferential direction [25]. In the case of the test foil bearing, the structural stiffness characteristics vary in the circumferential orientation as shown by Rubio and San Andrés [8]. However, due to the bump configuration in the axial direction, i.e. bump strips aligned and equally spaced, the structural stiffness does not have significant variations along the bearing axial length. In addition, static load measurements on the test foil bearings show nonlinear deflections, varying strongly with the orientation of the load relative to location of the foil spot weld [8].

In general, the static structural deformation of the top and bump foils depends on the design dimensional parameters, bearing preload magnitudes and test conditions under which the *FB* is excited such as load, frequency, amplitude of vibration, among others. Specifically, for the

current test foil bearings, the static structural behavior is well-known from static load versus deflection experiments performed by Rubio and San Andrés [8].

The test *FB*s were acquired from Foster-Miller Technologies in 2002. The *FB* manufacturer numbers are 047 and 043; and hereby referred as *FB1* and *FB2*, respectively. Figure 2 shows a photograph of the test foil bearing and Figure 3 portrays a detailed view of the test foil bearing components. Table 2 below presents the *FBs* main dimensions and geometry characteristics. The free-free and fixed-free bump stiffnesses are estimated using Iordanoff formulae [33].

Figure 2 Test bump type foil bearings
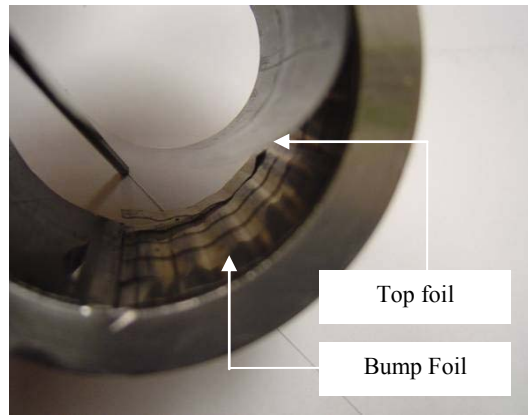
Figure 3 Detailed view of test foil bearing components

III.2. EXPERIMENTAL FACILITY DESCRIPTION

Figure 4 shows the test rig for rotordynamic experiments of a hollow rotor supported on foil gas bearings. The test rig consists of a hollow rotor supported on two bump-type foil bearings. A massive steel housing holds the test foil bearings in place and contains an internal duct to supply air pressure up to 0.70 MPa (100 psig) for cooling the test foil bearings while operating the test rig, if needed. The bearing housing also provides a direct access to the test rotor center location through a wide lateral groove. This feature allows the installation of an electromagnet (EM) load mechanism acting vertically at the test rotor center location. The function of the EM actuator is to apply a non-contacting load to the test rotor. Typical air gaps between EM tip and the test rotor vary from 0.25 mm (10 mil) to 0.50 mm (20 mil). The upper disk on the electromagnet mount allows a controlled vertical movement of the electromagnet to create various air gaps. As described in a later section, the EM actuator consists of a slender shaft made up of a high magnetic permeability material. The resulting non-contacting load originates from various

currents passing through copper wires wounded over the magnetic material. The following section of this report details more on the electromagnet load mechanism and its functioning.

Table 2 Nominal dimensions and parameters of test bump foil bearings

Parameters	SI Units	English Units
Inner diameter, ID:	38.17 mm	1.50 in
Outer diameter, OD:	50.80 mm	2.00 in
Axial bearing length, L:	38.10 mm	2.00 in
Radial nominal clearance[4], c_{nom}:	0.0355 mm	0.0014 in
Number of bumps, N_B:	25	
Bump pitch, p:	4.572 mm	0.18 in
Bump length, lo:	4.064 mm	0.16 in
Foil thickness, t_f:	0.102 mm	0.004 in
Bump height, h:	0.381 mm	0.015 in
Poisson's ratio, υ:	0.29	0.29
Bump modulus of elasticity, E:	213.73 MPa	31 Ksi
Bearing mass, M_B:	0.27 kg	0.61 lb
Free-free end bump stiffness[5], K_F	5.26×10^5 N/m	3.04 lb/mil
Free-fixed bump stiffness[5], K_W	8.76×10^5 N/m	5.06 lb/mil

---

[4] Nominal clearance for a 38.10 mm [1.500 in] diameter journal

[5] Bump stiffnesses are estimated using Iordanoff formulae [33].
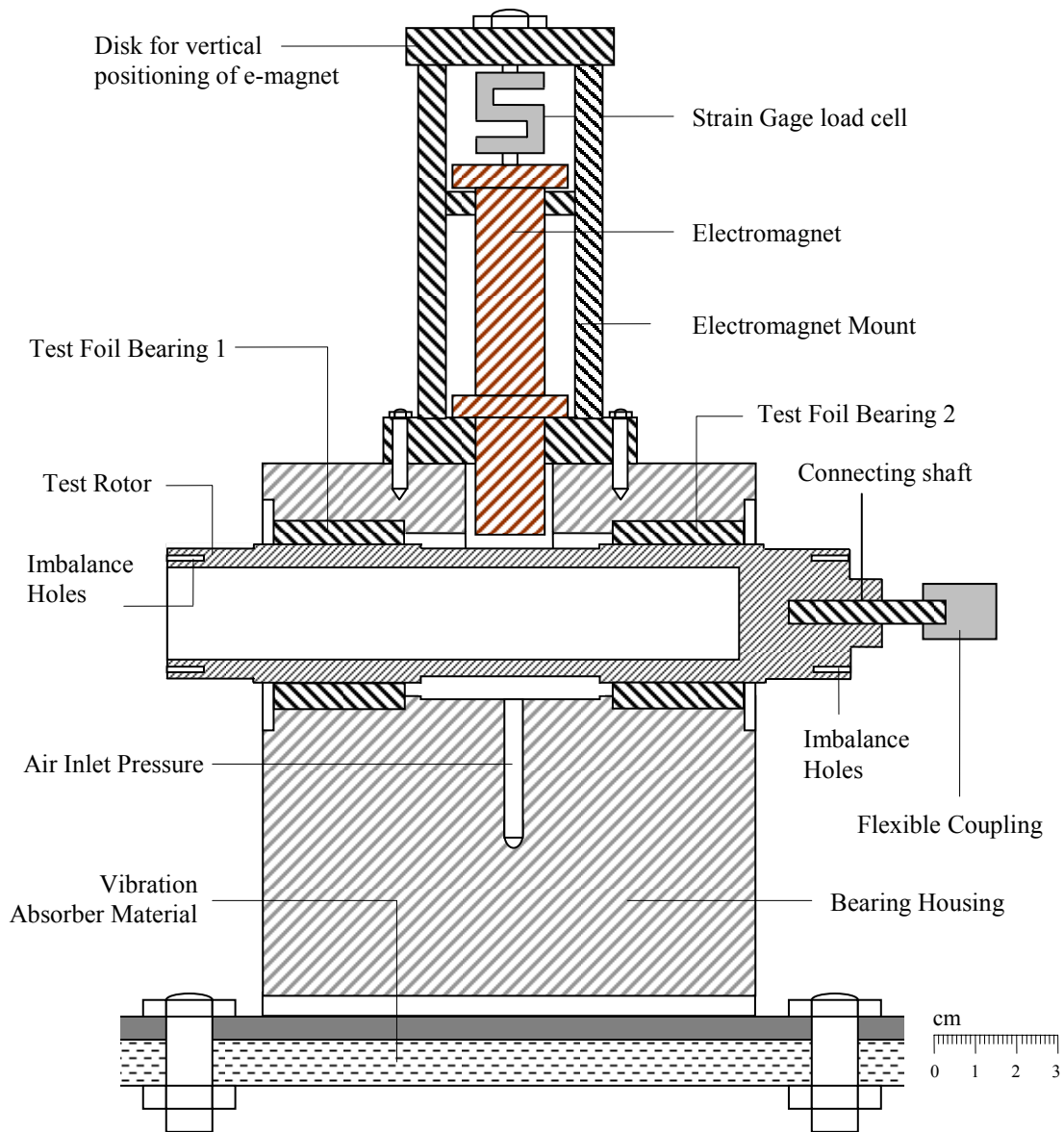
Figure 4 Test Rig for rotordynamic experiments of rotor supported on *FBs*

The test rotor, made of steel AISI 4140, consists of a hollow shaft of length 209.55 mm [8.25 in] and diameter at the bearing locations of 38.10 mm [1.500 in]. A TDC (thin dense chrome) coating, of thickness 25.4 μm [0.001 in], is applied to the test rotor surface at the bearing locations to improve friction and wear at the rotor/foil interface. Figure 5 shows details of the test rotor and main dimensions and Figure 7 shows a picture of the test rotor and foil bearings.

Table 3 presents a summary of the rotor inertia properties and geometry. The motor end has an internal thread to allow a coupling connection to the drive motor. Both rotor drive and free ends have 8 threaded holes where imbalance masses are attached at 15.11 mm (0.595 in) radius.
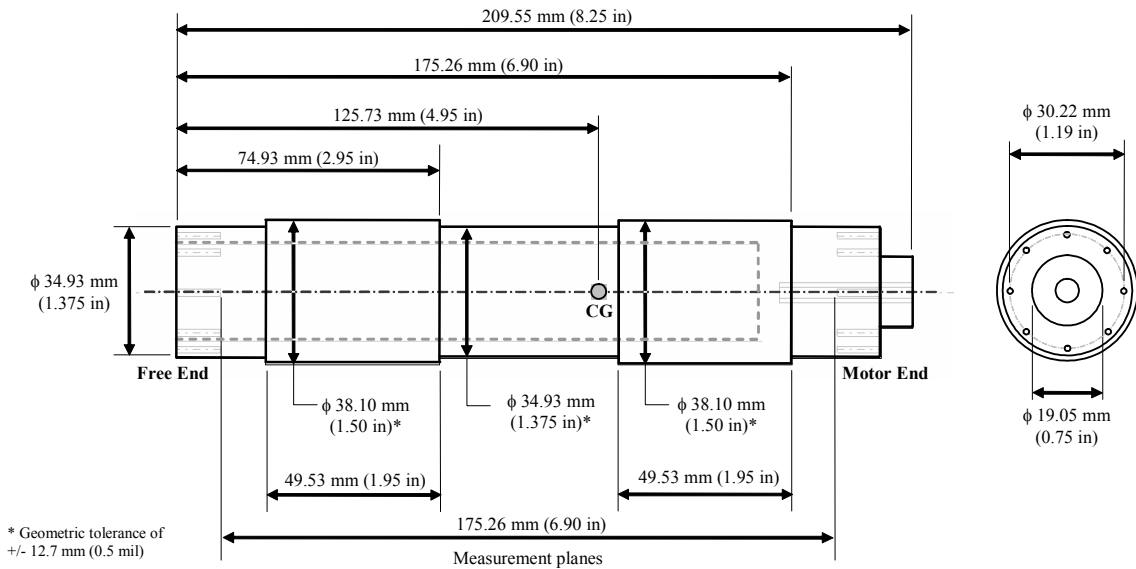
Figure 5 Geometry of test rotor (0.98 kg, 2.12 lb)

Shaft length = **209.5 mm** Shaft diameter at bearing locations =**38.10mm**
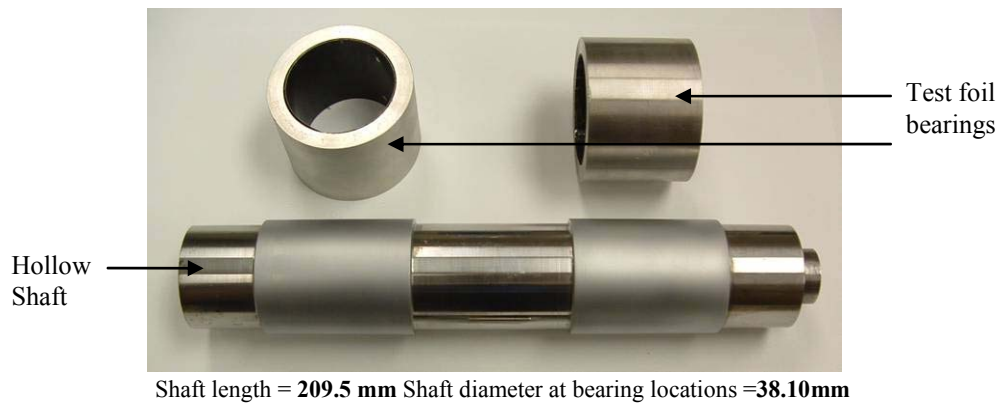
Figure 6 Test rotor and test foil bearings for rotordynamic tests

The first two free-free natural frequencies of the test rotor without the connecting shaft and the flexible coupling are at approximately 4096 Hz ± 127 Hz (245,760 rpm) and 9856 Hz ±127

26

Hz (591,360 rpm)[6]. Figure 7 shows predictions and experimental results of the mode shapes for the two free-free natural frequencies. The test results were obtained through free-free rap tests along the rotor axial length while the prediction were identified using a rotordynamic code (XLTRC^2®) developed in the Turbomachinery Laboratory at Texas A&M University. The free-free natural frequencies or bending critical speeds will not appear since the maximum test rig speed is 25,000 rpm. Rigid body natural frequencies without the connecting shaft and the flexible coupling are estimated through rap tests on the rotor supported on the test foil bearing. Appendix A explains the experimental procedure to estimate the rigid body natural frequencies and to identify structural bearing parameters.

Table 3 Summary of rotor geometry characteristics and inertia properties

Parameters	SI Units	English Units
Modulus of elasticity E	30 MPa	4.34 ksi
Material density, ρ	7830 kg/m^3	0.282 lb/in^3
Total mass[7], M	0.98 kg	2.2 lb
Diameter at the bearing locations[2], D with thin chrome coating	38.10 mm	1.50 in
Total length[2], L_T	209.55 mm	8.25 in
Distance between bearing locations[2], L_S	100.58 mm	3.95 in
Distance between the rotor CG to the free end, x_G	125.73 mm	4.95 in
Transverse moment of inertia, I_T	3.71x10^{-3} kg.m^2	12.67 lb.in^2
Polar moment of inertia, I_P	2.24x10^{-4} kg.m^2	0.76 lb.in^2

A Router motor, 1.49 kW [2.0 HP], drives the test rotor up to a top speed of 25,000 rpm[8]. The coupling connection for this motor/ test rotor configuration is through a miniature flexible coupling and a connecting shaft, see Figure 4. The connecting shaft, made of steel AISI 4140, comprises a threaded segment of length 38.1 mm [1.5 in] and a plain segment of length 12.7 mm

---

[6] Note that the addition of the connecting shaft and elastic coupling reduces the free-free natural frequencies to 1008 Hz and 3941 Hz as predicted by a finite element structural model. These frequencies are still above the maximum speed of test rig operation.

[7]The uncertainties on physical dimensions of the test rotor are within 3%.

[8]Attempts to operate the test rig with an air turbine (max speed 50 krpm) failed due to poor engineering and unscheduled installation difficulties.

[0.5 in] and diameter 5.08 mm [0.2 in]. The threaded segment connects with the test rotor while the plain section inserts into the flexible coupling. Figure 8 shows the single-disc flexible coupling geometry and major specifications.
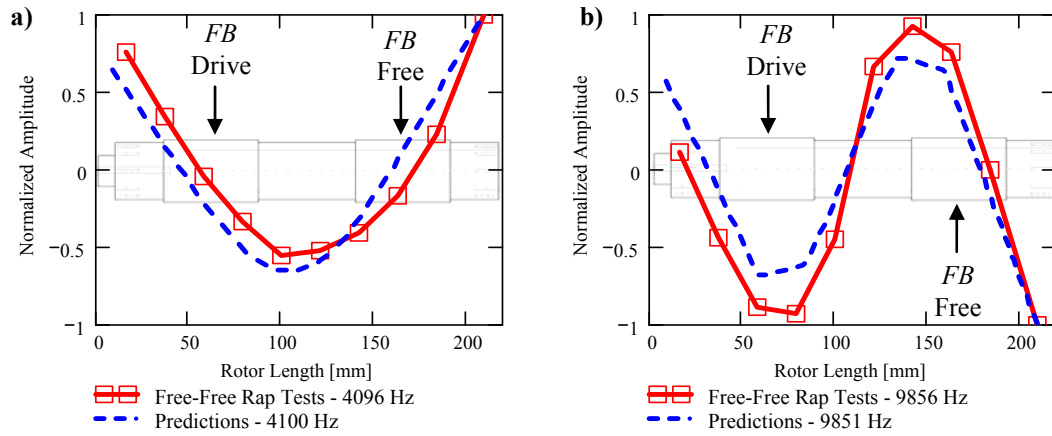
Figure 7 Predictions and Experimental Results of Free-Free Natural Frequencies, a) 4096 Hz ± 127 Hz and, b) 9856 Hz ± 127 Hz

Parameters	SI Units	English Units
Bores, ϕD_1 and ϕD_2	5.08 mm	0.20 in
Axial coupling length, A	31.00 mm	1.22 in
Hub length, C	9.00 mm	0.35 in
Hub major diameter, ϕB	15.00 mm	0.59 in
Transverse moment of inertia	3.0 gr.cm^2	1.02E^{-3} lb.in^2
Weight	9.0 gr	0.31 oz
Torsional stiffness	170 Nm/rad	15.2 lb.in/rad
Maximum speed	26,000 rpm	
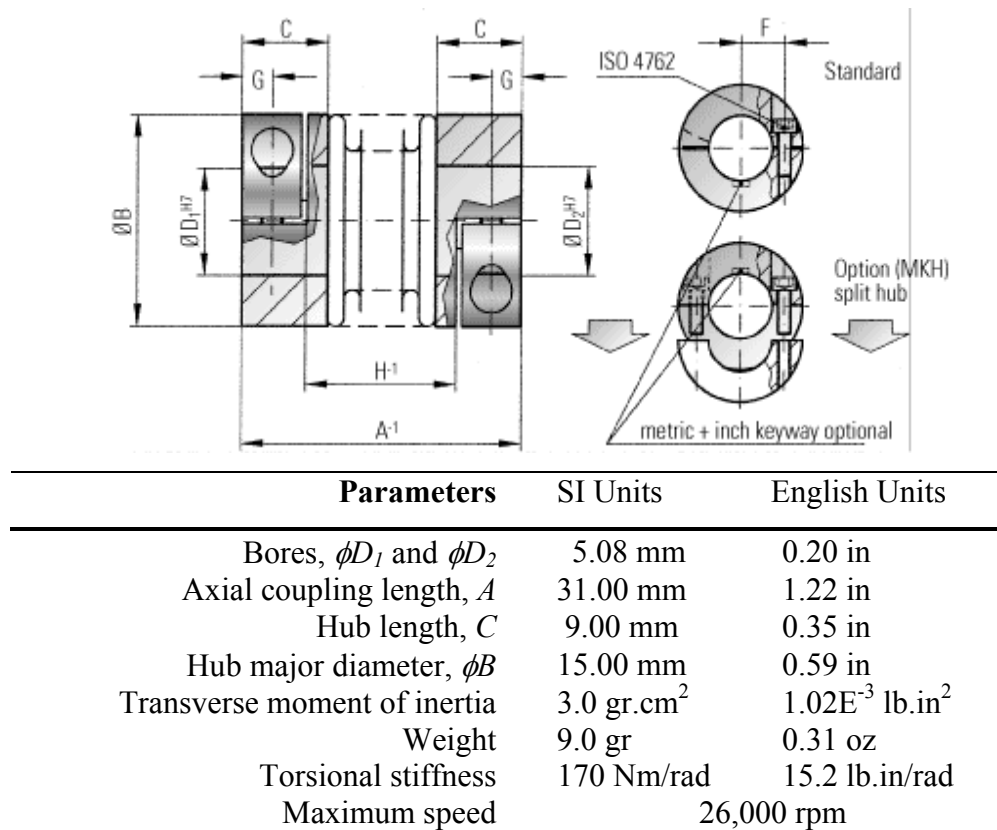
Figure 8 Miniature flexible coupling geometry and specifications.
Source: R+W Coupling website. http://www.rw-couplings.com

Measurements of the test rotor displacements are taken with two pairs of eddy current sensors located at the both rotor ends. The eddy current sensors measure vertical and horizontal displacements at the rotor measurement planes; see Figure 5. Vibration signals from the eddy current sensors connect to a signal conditioner to bias the DC offset levels and then into a commercial data acquisition system for industrial machinery monitoring and diagnostic (Bently Nevada, Adre DAQ system®). Table 4 summarizes the instrumentation sensors used for the rotordynamic test and the corresponding sensitivities. A two-channel dynamic signal analyzer displays the frequency content of the selected signals, and an analog oscilloscope displays the unfiltered rotor orbits in real time.

Table 4 Instrumentation installed in the *FB* test rig for electromagnet calibration and rotordynamic experiments

Measured magnitude	Instrument	Gain
Force, (y), vertical	Strain gage sensor	7.04 mV/N (31.0 mV/lb)
Displacement (X_{FE}), Free end horizontal	Eddy current sensor	7.84 mV/micron (199.2 mV/mil)
Displacement (X_{DE}), Drive end horizontal	Eddy current sensor	7.80 mV/micron (198.3 mV/mil)
Displacement (Y_{FE}), Free end vertical	Eddy current sensor	7.48 mV/micron (190.2 mV/mil)
Displacement (Y_{DE}), Drive end vertical	Eddy current sensor	7.88 mV/micron (200.3 mV/mil)

Figure 9 shows a picture of the instrumentation rack used to monitor and record test data of the test rig. The strain gage force sensor connects the electromagnetic actuator to a fixed vertical-positioning disk, see Figure 4. Therefore, the strain gage meter readings represent electromagnetic forces acting on the test rotor. An optical sensor aligned along the horizontal direction provides a reference signal for measurement of the phase angle and rotor speed. A personal computer receives the measured signal data and runs the signal processing and analysis software.
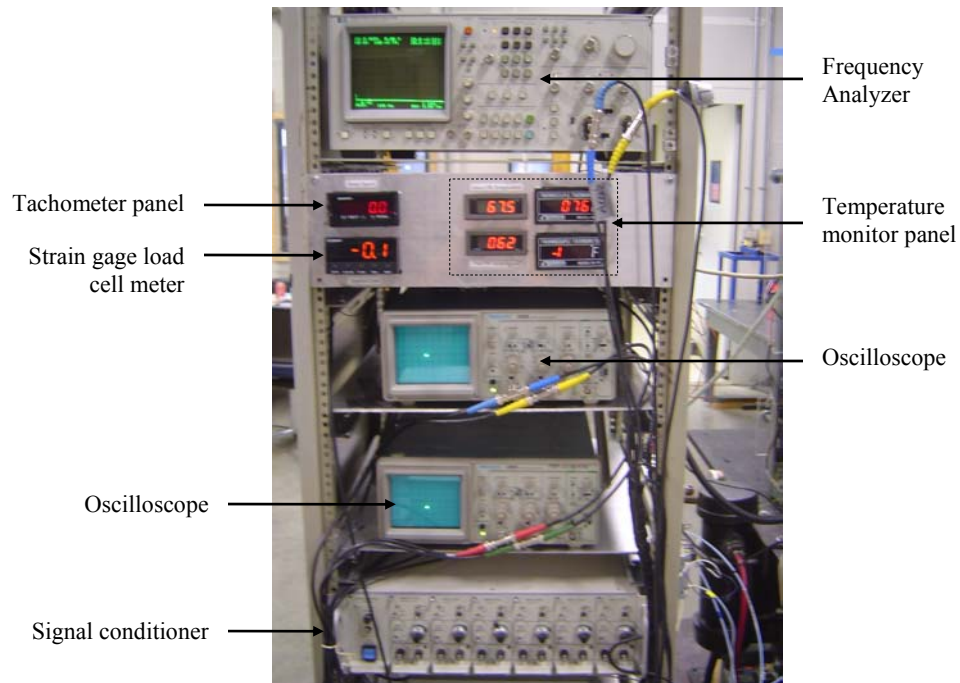
Figure 9 Picture of the instrumentation rack used for *FB* testing

While operating the test rig, the temperatures on the outer surface of the test foil bearings are monitored, as shown in Figure 10. Also, as a result of the continuous current through the electromagnet cables, heat is generated and temperature on the electromagnet surface rises. A thermocouple monitors the temperature variation on the electromagnet surface. Due to excessive temperature rise on the electromagnet surface a cooling system is implemented to dissipate the generated heat. This is ensured by a series of copper tubes wounded over the electromagnet with cool oil flowing through the tubes. Appendix B details fully on the cooling system for the electromagnet as well as the electromagnet load mechanism and its functioning.
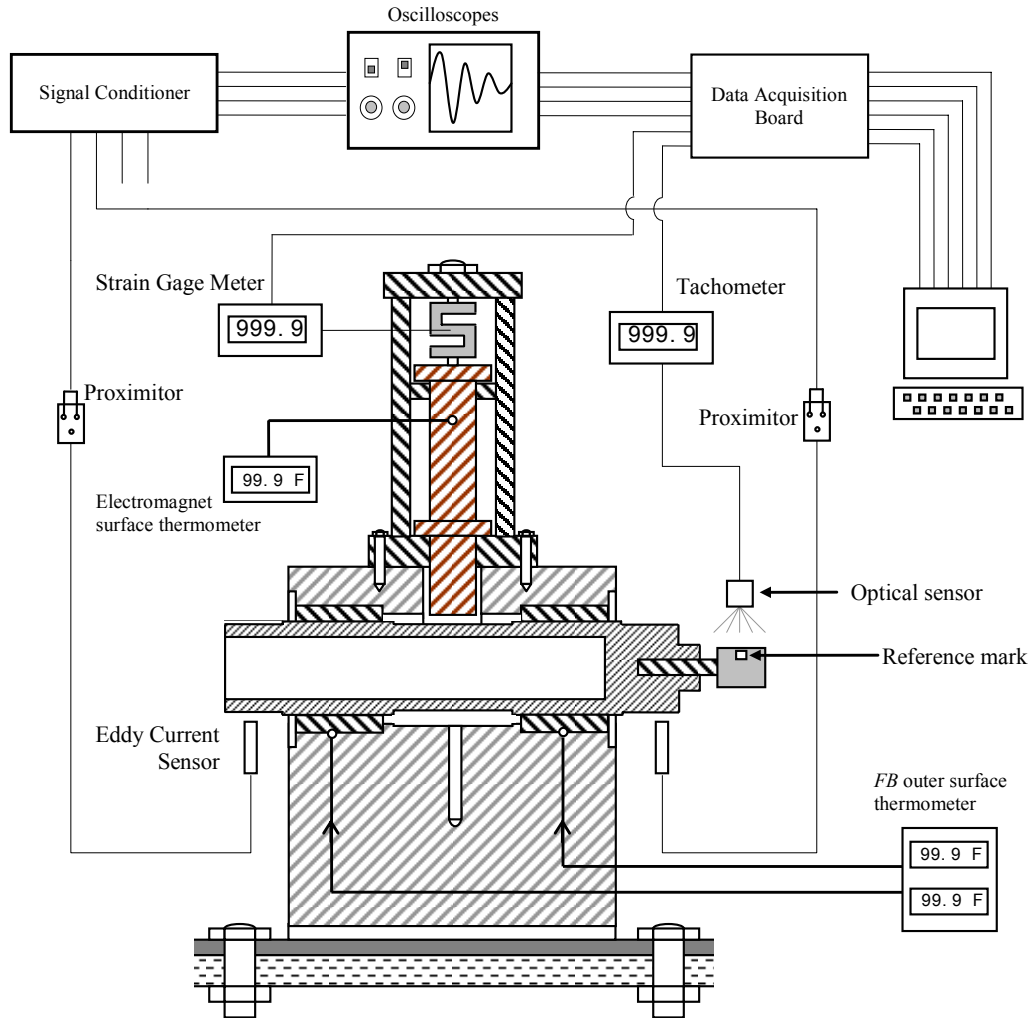
Figure 10 Data acquisition system for measurement and recording of rotor vibration, applied electromagnet force and rotor speed

III.3. NOMINAL IMBALANCE CONDITION OF TEST ROTOR

Rotor balancing is important because it provides a baseline for measurement of rotor response to calibrate imbalance masses. For the test rotor, a standard influence coefficient method for two-plane balancing substantially reduces the original rotor synchronous response to satisfactory small levels of vibration. The selected speed for the balancing procedure is 4,000 rpm, well below the first critical speed at ~ 9,000 rpm. The rotor balancing procedure consists of introducing imbalance masses at the rotor free and motor drive ends. The ensuing synchronous motion vectors (amplitude and phase), vertical and horizontal directions, at the rotor free and drive end are recorded. The imbalance mass and the angle between the trial mass and tachometer

position, coinciding with the reflective surface in the rotor, represents the imbalance mass vector. The angles are considered positive against shaft rotation.

Once the rotor balancing tests are performed, the influence coefficient method allows determination of correction mass vectors (amplitude and angular location) to balance the test rotor. Figure 11 shows the location and magnitudes of the calculated correction weights at the free and motor end. Once the correction weights are inserted, the test rotor is brought to its maximum speed (25 krpm) and the baseline condition is recorded at the four rotor locations.
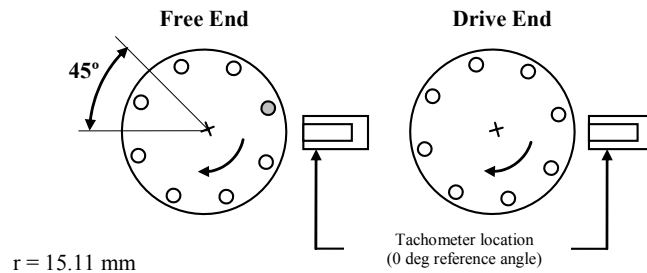
Correction Masses	Drive end	Free end
Distributed correction mass	None	3.62 gr.mm @ 27º

Figure 11 Correction weight magnitudes and angular positions at the balancing planes

Figure 12 and Figure 13 show the amplitudes of the direct and synchronous coastdown displacement responses (zero to peak) of the rotor baseline condition for a supply pressure at the bearing housing midspan of 34.4 kPa [5 psig][9]. The baseline synchronous responses in Figure 13 show subtraction of the runout vector at the lowest running speed, i.e. ~ 1500 rpm.

Rotor displacement designations are: X_{DE} for horizontal drive end, Y_{DE} for vertical drive end, X_{FE} for horizontal free end, and Y_{FE} for vertical free end.

---

[9] Imbalance response tests for increasing supply pressures are shown later.
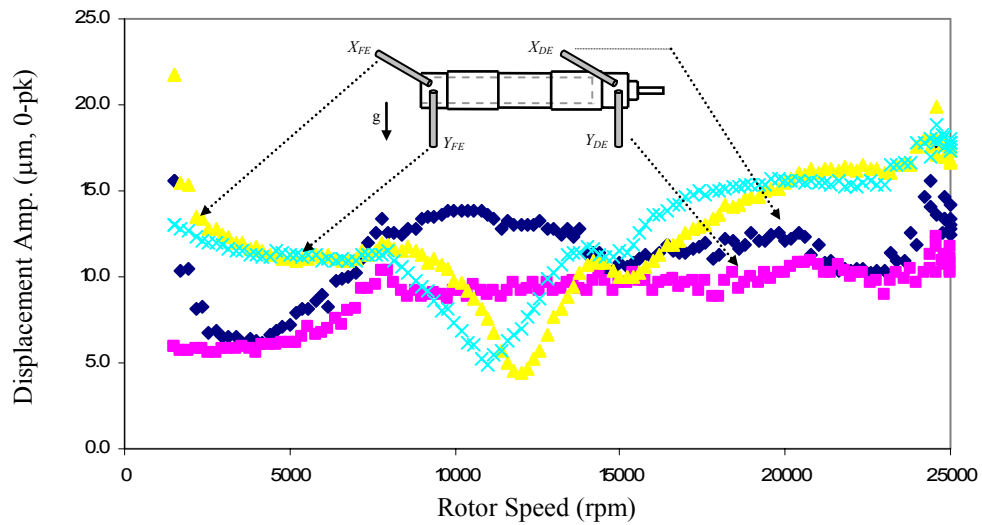
Figure 12 Direct displacement response of the rotor <u>baseline condition</u> for air supply pressure equal to 34.4 kPa [5 psig]

The direct response comprises the synchronous and non-synchronous contents of the rotor response. Non-synchronous vibration components occur at low shaft speeds due to the dry friction generated from the journal and top foil upon contact. Notice that the synchronous components of baseline condition are not small (< 20 μm).
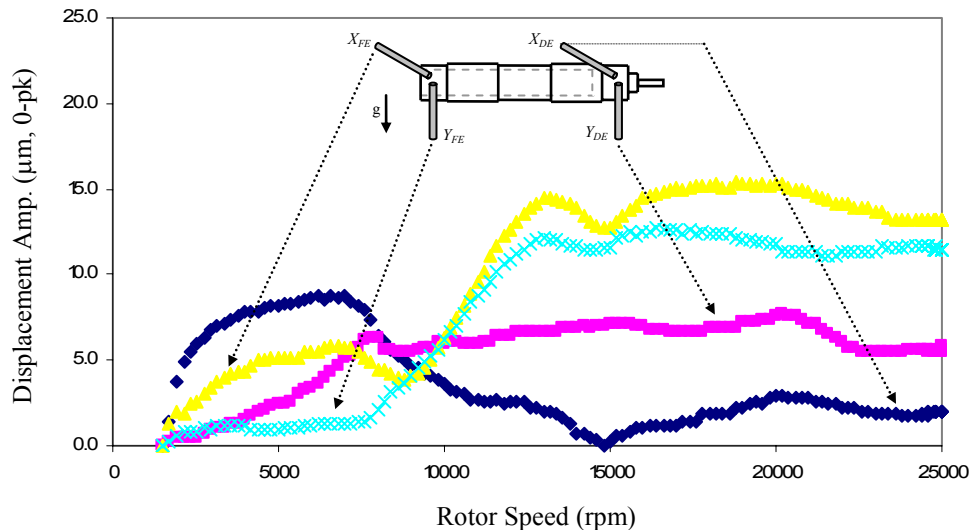
Figure 13 Synchronous displacement responses of the rotor <u>baseline condition</u> for air supply pressure equal to 34.4 kPa [5 psig]

Figure 14 and Figure 15 present waterfall plots of the baseline rotor coastdown response along the horizontal direction for the rotor drive end and free end, respectively. Appendix C shows waterfall plots for the other two measurement locations. Low magnitudes of super-harmonics motions compared to the synchronous magnitudes are noted over the entire shaft speed range. Incipient subsynchronous vibration for the baseline condition is observed at the maximum speed (~ 25 krpm). The frequency of subsynchronous whirl is approximately at the rigid body mode natural frequency (~9,000 rpm (150 Hz)). For shaft speeds lower than 20,000 rpm, the subsynchronous components disappear indicating that the system is stable (no whirl).
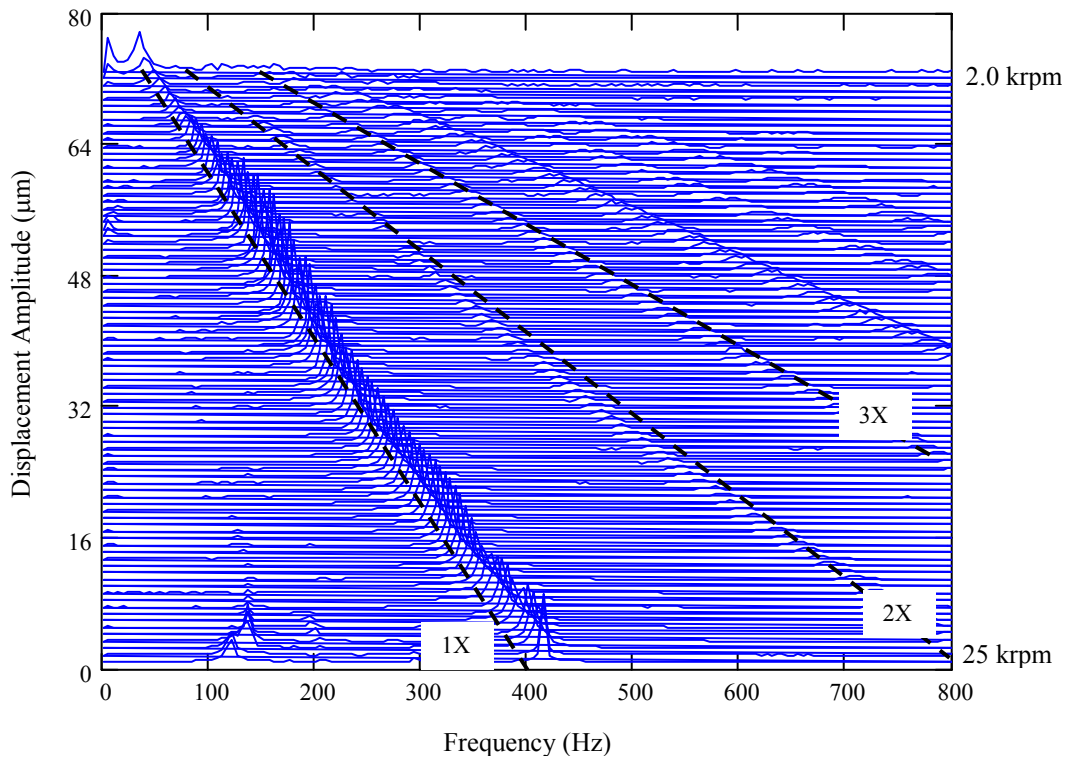
Figure 14 Waterfall plot of baseline rotor coastdown at drive end, horizontal plane (X_{DE}). Air pressure at 34.4 kPa [5 psig]
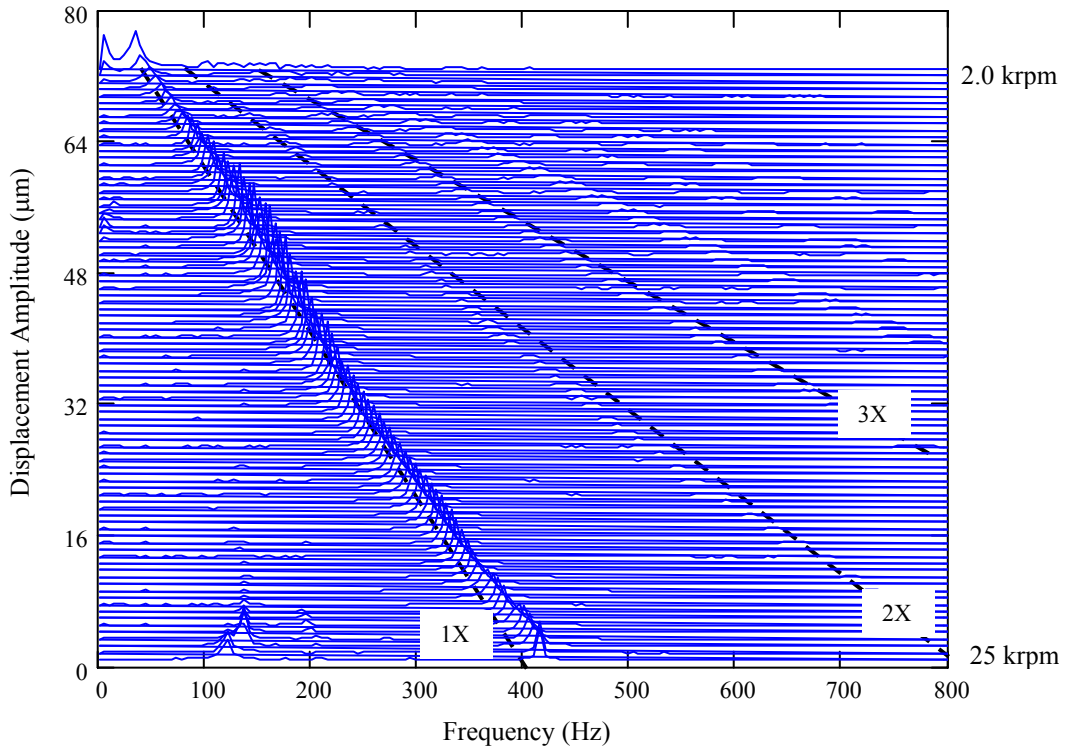
Figure 15 Waterfall plot of baseline rotor coastdown at drive end, vertical plane (Y_{DE}). Air pressure at 34.4 kPa [5 psig]

IV. ESTIMATION OF CLEARANCE IN FOIL BEARINGS

The estimation of the clearance for the test foil bearings is paramount to correlate experimental results with analytical predictions. An ad-hoc experimental procedure is performed to estimate the test bearing clearances. The procedure consists of placing calibrated shims of thickness 25.4 μm and 50.4 μm between the journal and the test foil bearings and recording the ensuing rotor vertical displacement. Then, a simple algebraic formulation allows the estimation of the bearing clearances. Figure 16 shows a schematic view of the experimental procedure where the estimated bearing clearance (*c*) is given by the following expression,

$$c = g - \delta_{static} \tag{1}$$

where, *g* is the initial air gap and δ_{static} is the resulting bearing static deflection due to the fraction of rotor weight supported. Once the shims are inserted, the ensuing rotor displacement is recorded and the initial air gap is estimated as,

35

$$g = S - \delta_S \tag{2}$$

where, S is the shim thickness and δ_S is the rotor displacement, i.e. $\delta_S = \delta_{S2} - \delta_{S1}$.

Figure 16 Schematic representation of procedure to estimate bearing clearance

The fraction of static rotor weight supported by each bearing and the foil bearing structural stiffness determine the static bearing deflection (δ_{static}). The static rotor weight supported by each bearing is estimated through a simple balance of static forces on the rotor/bearing system, i.e. 7.35 N and 2.45 N for the drive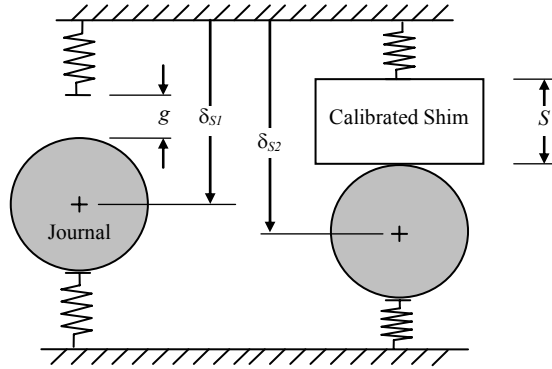 end and free end foil bearings, respectively. The foil bearing structural stiffness is obtained from experimental and analytical results given in [8].

Figure 17 provides predicted and experimental values of structural stiffness for a shaft diameter of 38.10 mm with no preload. Notice also that the figure contains the predicted value of a single bump stiffness with only one fixed end[10]. Figure 17a also provides an inset of the structural stiffness for a static load range comprising the fraction rotor weight at the bearings. Table 5 provides the corresponding stiffness values for each foil bearing. The test bearing configuration features a <u>spot weld line</u> at the bottom of the bearing. Recall that the test foil bearing design presents a spot weld where the top foil attaches to the bearing sleeve, and four spot weld lines where the bump strips are affixed at the bearing sleeve.

Estimated values of *FB* structural stiffnesses due to the fraction rotor weight correspond to specific values of bearing static deflection (δ_{static}). These deflection values are obtained from experimental and analytical results of structural stiffness versus bearing deflection curves advanced in [8]. Table 5 presents the values of static deflection for both bearings.

---

[10] Single bump stiffness is determined using Iordanoff's formulae [33].
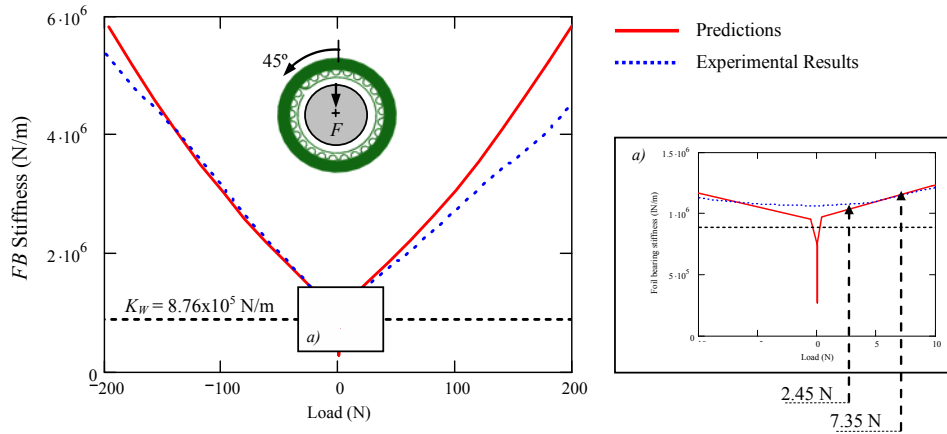
36

Figure 17 Predicted and experimental structural stiffness varying with static load for a shaft diameter of 38.10 mm and no bearing preload. Results obtained for spot weld located at 45° of top vertical axis

Once the static bearing deflection is determined, Equation (1) estimates the bearing clearances for initial air gaps calculated in Equation (2). The procedure to estimate bearing clearance assumes no bump deflection at the top of the bearing once the shim is inserted. Table 5 presents the estimated values of bearing clearances obtained using a shim of thickness 50.8 μm. No rotor displacement is detected when using a shim of thickness of 25.4 μm. Recall that the shim is inserted individually at each bearing and the ensuing rotor displacement is recorded at the rotor end where the shim is inserted. Notice that the estimated bearing clearances are about half the nominal clearance given by the manufacturer. The differences between the nominal and estimated clearances may be attributed to inaccuracies on the test *FB* diameter and shaft diameter. The clearances reported in Table 5 are rough estimates of the actual ones, which should be more properly determined from static load tests and more accurate instrumentation.

Table 5 Estimation of bearing clearance using a shim of thickness 50.8 μm [2 mil]

Parameters	Free end foil bearing	Drive end foil bearing
Static weight, W_b	2.45 N	7.35 N
Static deflection, δ_{static}	4.2 μm	13.6 μm
Shaft displacement, δ_S	1.9 μm	3.2 μm
Air gap, g	48.8 μm	47.6 μm
Diametral clearance, $2c$	**44.6 μm**	**34.0 μm**
Nominal clearance, $2c_{nom}$	70.0 μm	70.0 μm

37

V. IMBALANCE RESPONSE TESTS

Imbalance response tests were conducted with calibrated imbalance masses at the two imbalance planes in the rotor. The distribution of masses leads to two linerly independent responses of the test rotor. For each rotational speed, the baseline condition is subtracted from the measured imbalance response to reveal the actual effect of the mass imbalance used[11]. The imbalance responses, presented herein, are for rotor coastdowns from 15,000 rpm[12]. Table 6 summarizes the magnitude and location of the imbalance masses for the two types of imbalance tests, A and B. In tests A, the imbalance masses are added at the same angular location at the rotor end planes; whereas in tests B, the imbalance masses are out of phase (180°). For each imbalance condition, an imbalance displacement (u) is defined as

$$u = \frac{\left| m_{FE} . r_e . e^{i\phi_{FE}} \right| + \left| m_{DE} . r_e . e^{i\phi_{DE}} \right|}{M + m_{DE} + m_{FE}}$$

(3)

where, m_{FE} and m_{DE} are the imbalance masses at the free and drive end, respectively, ϕ_{FE} and ϕ_{DE} are the imbalance mass locations at the free and drive end, respectively, M is the rotor mass ($M = 1$ kg), and r_e is the radial distance of the imbalance location (15.11 mm).

Figure 18 shows direct and synchronous coastdown responses at the four measurement locations for imbalance displacement $u = 7.4$ μm (in phase, test A1). Small non-synchronous vibrations are encounter throughout the entire speed range for this smallest imbalance condition. Rotor motions at the drive end evidence the occurrence of a critical speed at ~ 8.2 krpm while motions at the free end do not manifest this critical speed. Later, analysis of the phasor vectors[13] at the measured displacement signals determine the rigid body shape associated to this critical speed, i.e. cylindrical or conical. Figure 19 displays direct and synchronous coastdown responses for a large imbalance displacement, i.e. $u = 10.5$ μm (in phase). Synchronous magnitudes for all measurement locations indicate a clear critical speed occurring at 8.2 krpm. On the other hand, nonsynchronous motions initiate at 20.5 krpm and disappear at 12 krpm. This speed range

---

[11] The procedure is strictly correct in a linear system.

[12] The repeatability of test results is significantly better for coastdowns from 15 krpm than those starting from 25 krpm. The lower start speed for coast downs avoids excessive build up of subsynchronous motions.
[13] The phasor vector contains the amplitude and phase angle of the time measured signals.

encloses a speed twice the system first critical speed. Sub-synchronous vibrations are also observed near the critical speed. A following section presents waterfall plots for this imbalance condition showing the frequencies at which these non-synchronous vibrations occur. Figure 18 and Figure 19 indicate that subsynchronous vibrations are more notorious when imbalance masses are the largest.

Table 6 Imbalance mass magnitudes and locations

Imbalance Name	Imbalance mass $(m_{FE} / m_{DE}) \pm 0.002$ g	Imbalance mass location (ϕ_{FE} / ϕ_{DE})	Imbalance displacement (u)
A1	0.24 g / 0.24 g	-18° / -18°	$u = 7.4$ μm
A2	0.31 g / 0.31 g	-18° / -18°	$u = 9.5$ μm
A3	0.34 g / 0.34 g	-18° / -18°	$u = 10.5$ μm
B1	0.12 g / 0.12 g	-18° / 162°	$u = 3.7$ μm
B2	0.17 g / 0.17 g	-18° / 162°	$u = 5.2$ μm
B3	0.24 g / 0.24 g	-18° / 162°	$u = 7.4$ μm

Free and drive end imbalance plane: radius = 15.11 mm
Positive angles <u>on rotor</u> are measured opposite to direction of rotation and from rotating reference, i.e. reflective pick-up mark.
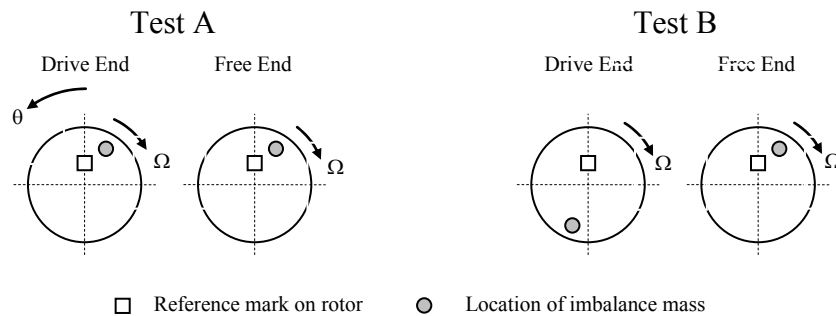
As noted earlier, the rotor response is recorded at the measurement planes noted in Figure 5. However, a simple geometrical transformation assuming rigid rotor motion allows determining the rotor imbalance response at the bearing locations. Appendix D shows the direct and synchronous coastdown responses at the bearing locations and a comparison with the identified bearing clearances.

Figure 18 Direct and synchronous coastdown response for an imbalance displacement of
u = 7.4 μm (in phase, Test A1). Air pressure at 34.4 kPa [5 psig]

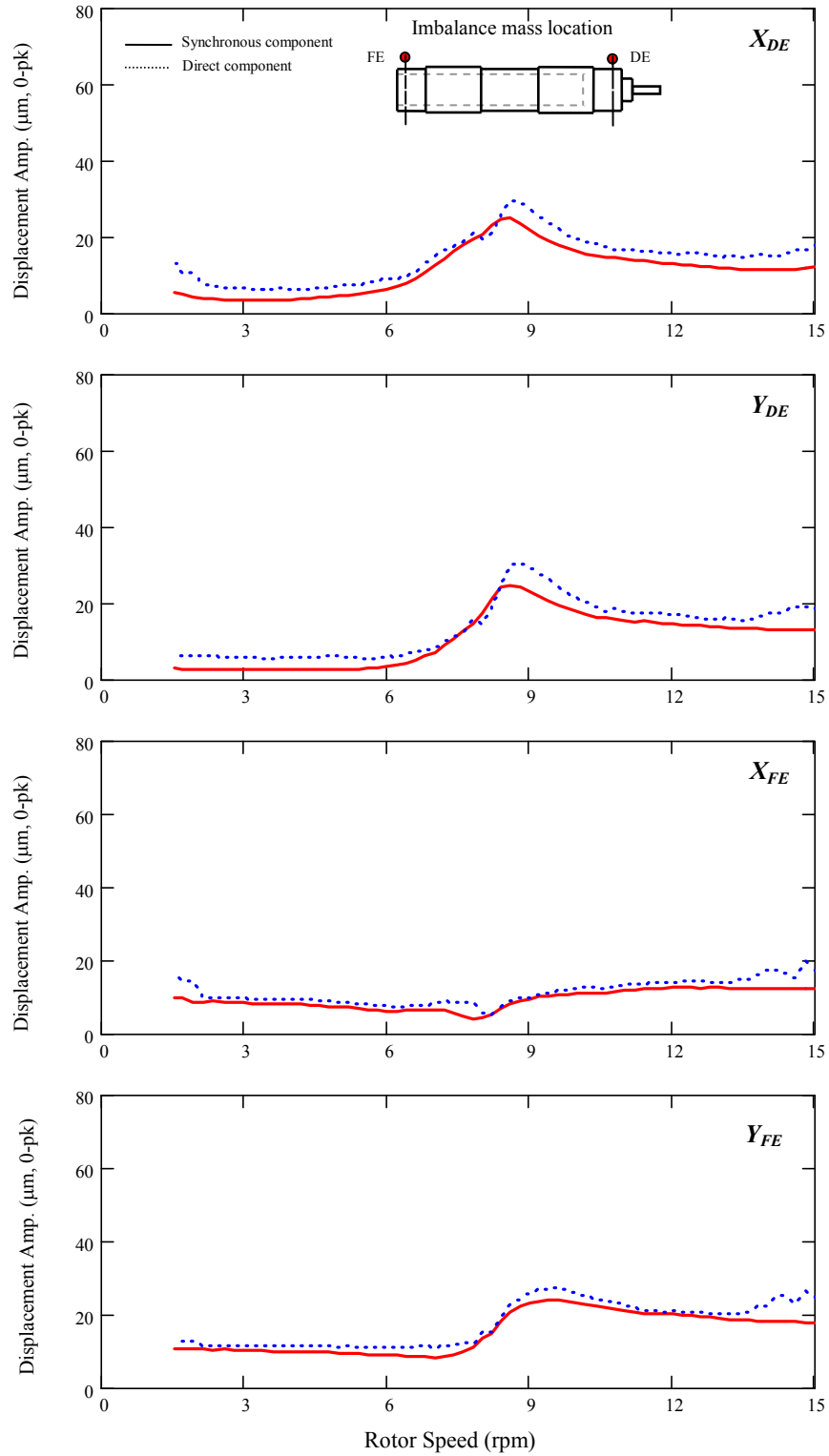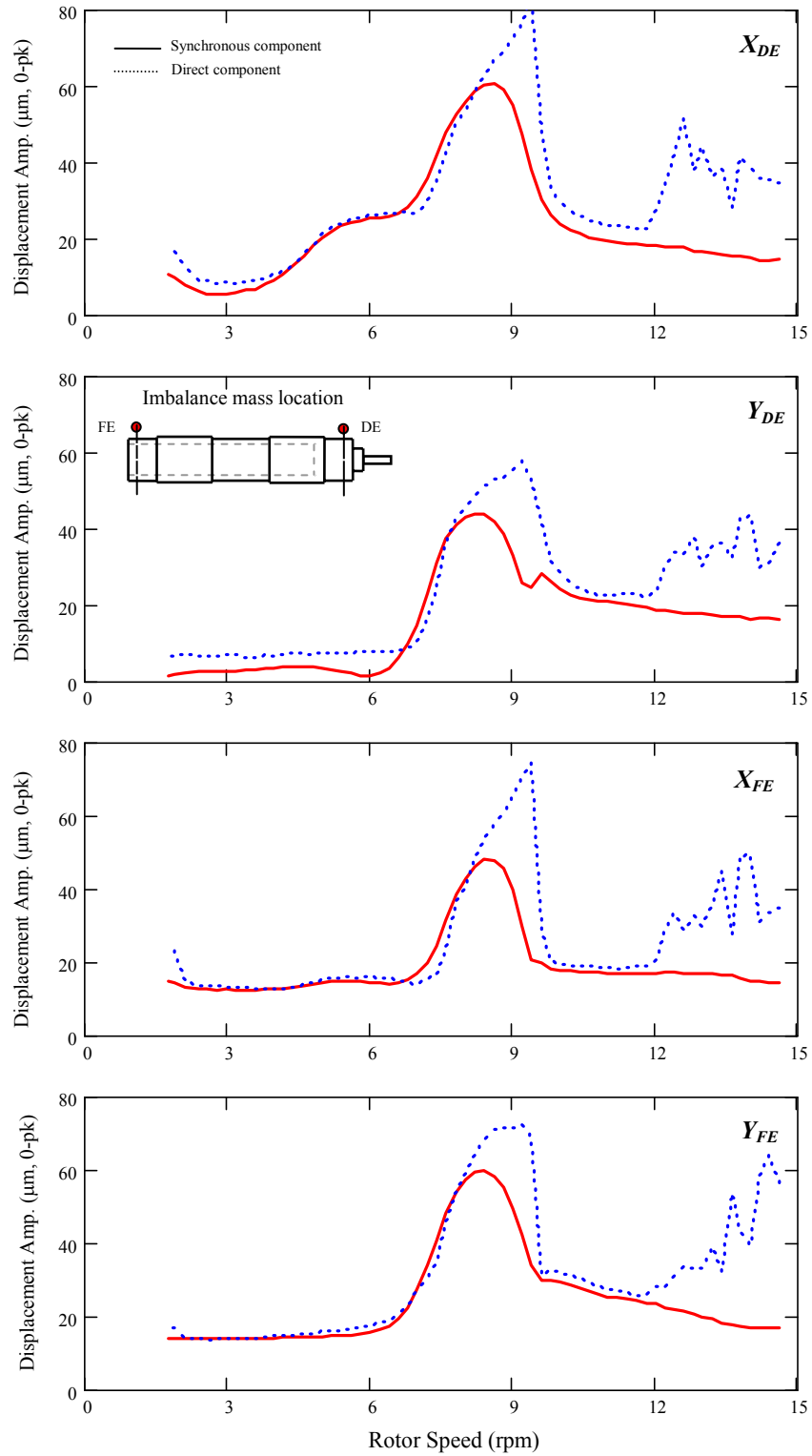**Figure 19 Direct and synchronous coastdown response for an imbalance displacement of u = 10.5 μm (in phase, Test A3). Air pressure at 34.4 kPa [5 psig]**

Similarly, Figure 20 presents synchronous and direct coastdown responses for an imbalance displacement of $u = 5.2$ μm (out of phase). In general, subsynchronous vibrations initiate at twice the system critical speed and disappear at approximately 12.5 krpm.

The two distinctive imbalance tests allow identification of the first two rigid body mode critical speeds. From imbalance tests A, the first critical speed is at approximately 8.2 krpm; while from imbalance tests B, the second critical speed occurs at approximately 9.0 krpm. Note that for imbalance tests B, the first rigid body mode critical speed is excited at the horizontal drive end location while at other locations the second rigid body mode is excited.

Figure 21 through 24 present synchronous rotor responses for increasing imbalance masses. Recall that the imbalance responses show the subtraction of the baseline condition. Figure 21 and Figure 22 depict measured responses at the rotor drive end and free end (horizontal plane), respectively, for imbalance tests A. Experimental results in Figure 23 and Figure 24 correspond to imbalance tests B at the rotor drive and free ends (vertical plane), respectively. In general, amplitudes of rotor synchronous motions (1X) at the critical speeds augment in an approximately linear manner as the imbalance mass increases. Appendix E verifies the linearity of the test rotor bearing system for the various imbalance conditions. Amplitudes of synchronous motions (1X) are largely different for vertical and horizontal rotor motions, thus evidencing the anisotropy of the test foil bearings. Recall that the test foil bearings are installed with the spot weld at 45º clockwise from the top vertical orientation.

Figure 21 through Figure 24 also show the phase angle changes of the measured signals for the entire speed range. A clear shift in the phase angle near the two first critical speeds is distinguished for all imbalance conditions.

Appendix F shows the synchronous and direct rotor responses for the remaining imbalance conditions, i.e. A2, B1, and B3 (refer to Table 6 for imbalance displacement magnitudes). Appendices G and H show the synchronous responses and phase angles at the locations not shown in this section for imbalance tests A and imbalance tests B, respectively.
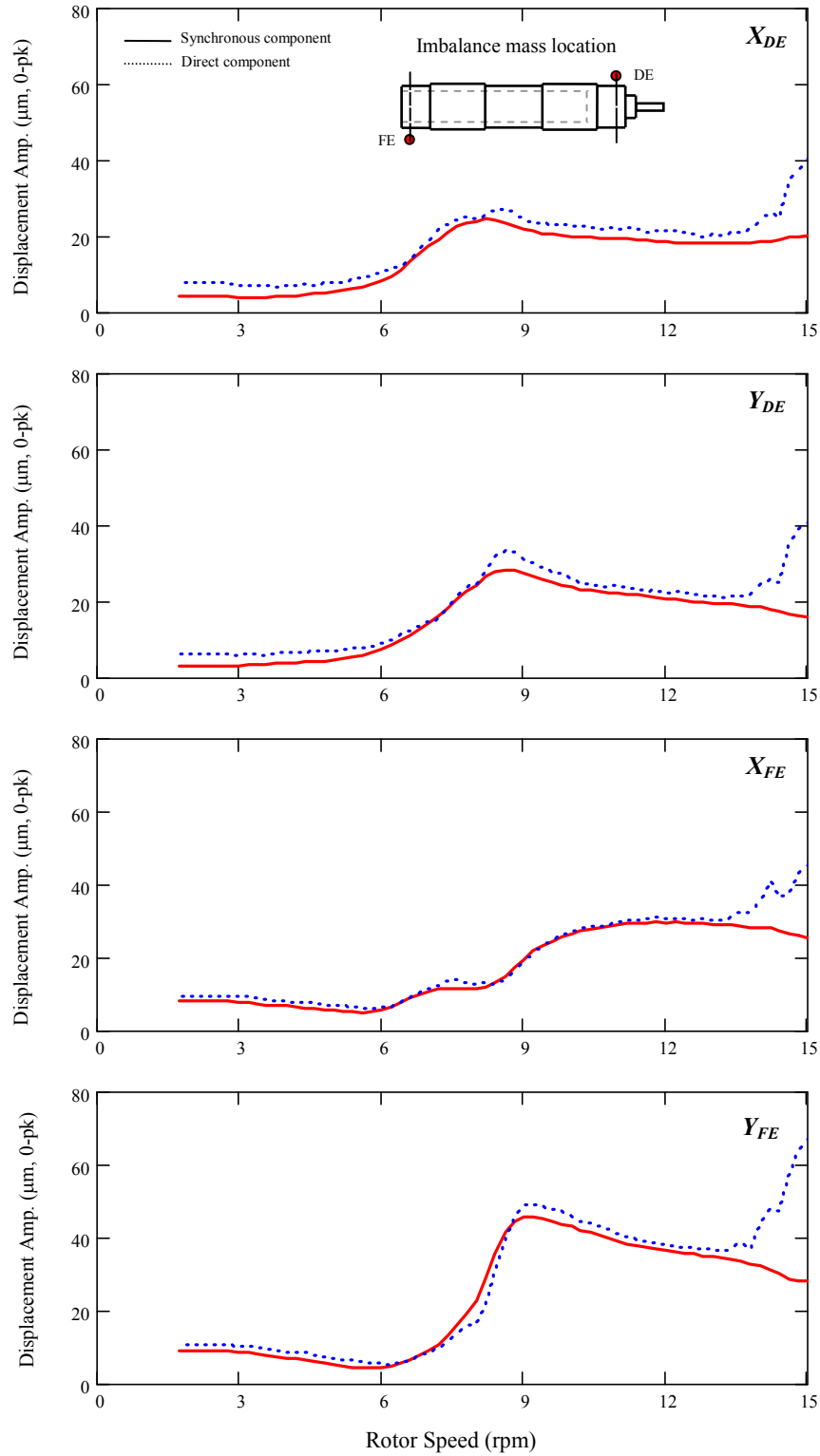
Figure 20 Direct and synchronous coastdown response for an imbalance displacement of
u = 5.2 μm (out of phase, test B2). Air pressure at 34.4 kPa [5 psig]

Figure 21 Synchronous rotor response amplitude and phase angle for imbalance tests A. Air pressure at 34.4 kPa [5 psig]. Measurements taken at drive end, horizontal direction (X_{DE})

Figure 22 Synchronous rotor response amplitude and phase angle for imbalance tests A. Air pressure at 34.4 kPa [5 psig]. Measurements taken at free end, horizontal direction (X_{FE})

Figure 23 Synchronous rotor response amplitude and phase angle for imbalance tests B. Air pressure at 34.4 kPa [5 psig]. Measurements taken at drive end, vertical direction (Y_{DE})

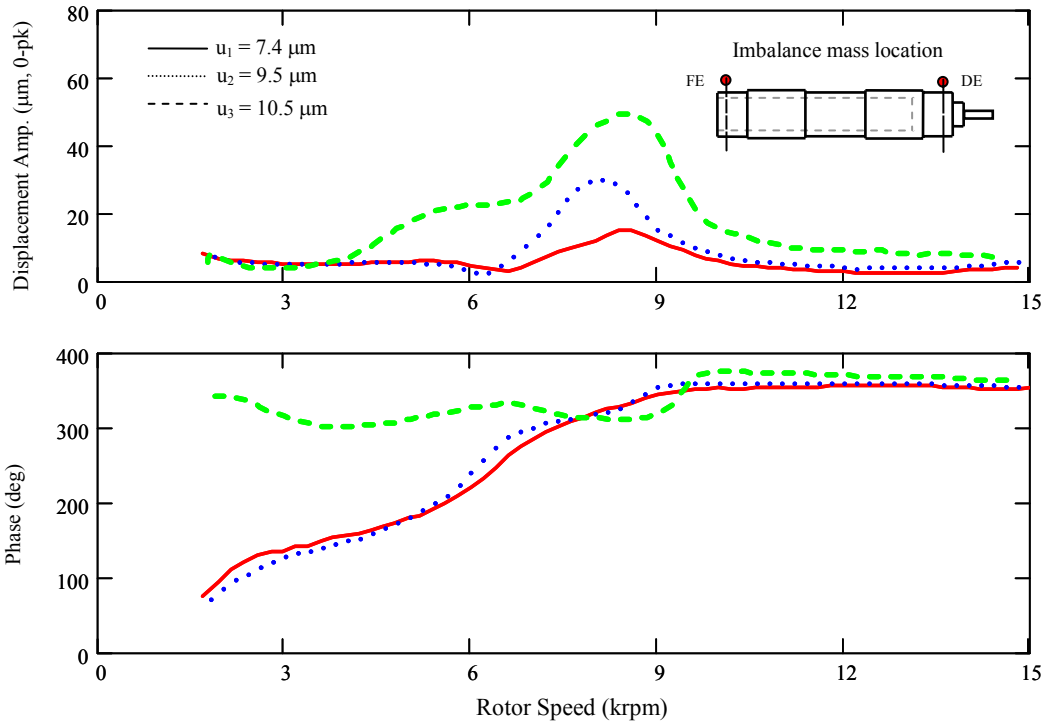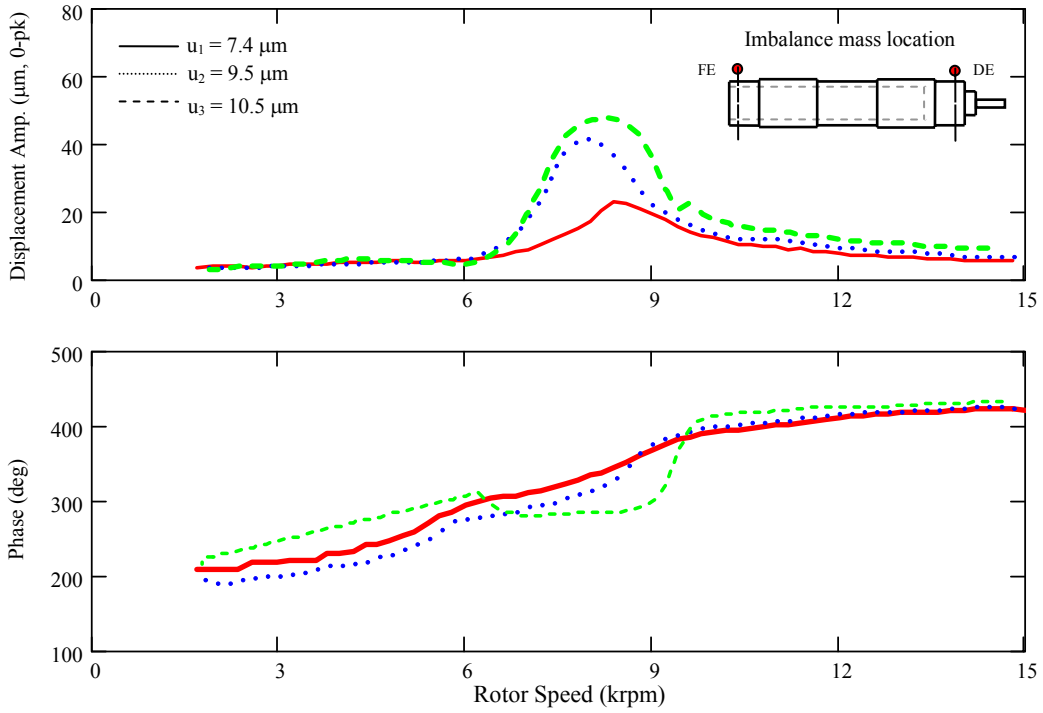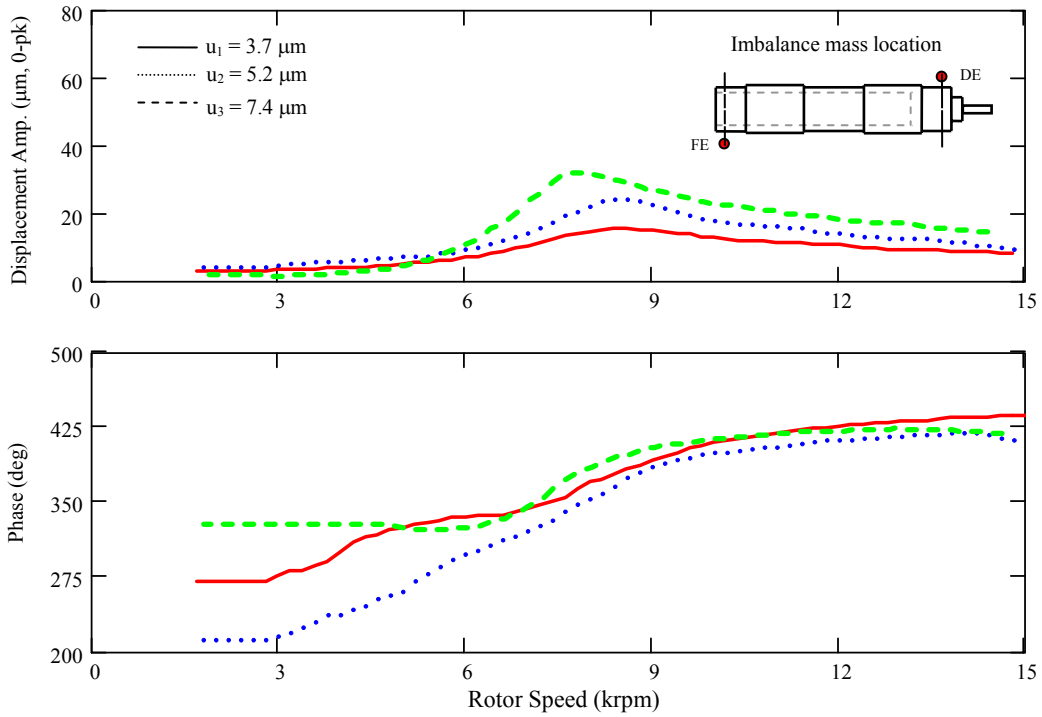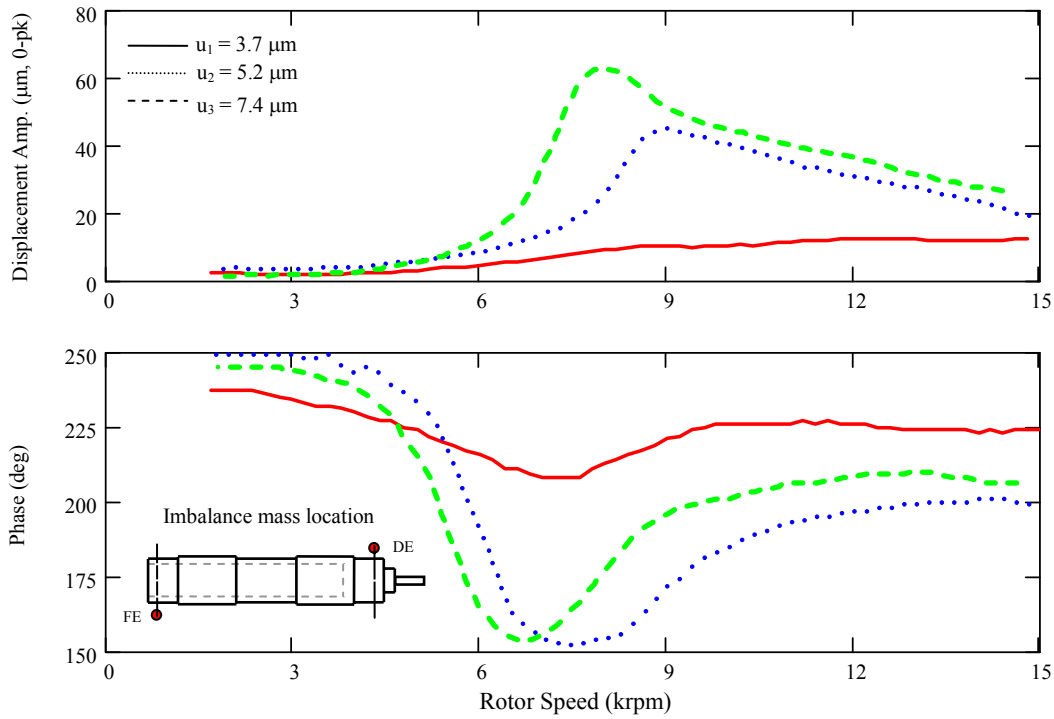**Figure 24 Synchronous rotor response amplitude and phase angle for imbalance tests B. Air pressure at 34.4 kPa [5 psig]. Measurements taken at free end, vertical direction (Y_{FE})**

VI. WATERFALL ANALYSIS OF COASTDOWN ROTOR RESPONSES

Synchronous and subsynchronous vibrations of coastdown tests from 25,000 rpm are analyzed below. Waterfall plots are presented for imbalance displacements u = 7.4μm (in phase), u = 10.5 μm (in phase), and u = 5.2 μm (out of phase). Figure 25 shows a waterfall plot of the rotor coastdown response for an imbalance displacement of u = 7.4μm (in phase). Figure 26 displays the corresponding synchronous and subsynchronous components and the whirl frequency ratio (WFR). The WFR is defined as the ratio of subsynchronous frequency to the shaft angular frequency. In general, synchronous motion dominates the rotor response for the entire coastdown speed range, i.e. 25 krpm to 2 krpm. Recall that the imbalance rotor responses presented in the previous section relate to coast downs from 15 krpm; whereas the waterfall plots are obtained for coastdowns from 25 krpm. Therefore, experimental results from both set of experiments may differ due to lack of repeatability for coastdowns starting from different initial speeds.

Figure 27 depicts waterfall plots of the rotor coastdown response for an imbalance displacement of u = 10.5 μm (in phase). Subsynchronous motions exist from ~ 20.5 krpm to 15.0 krpm with a 50% typical whirl frequency ratio, see Figure 28. Below 15 krpm, the subsynchronous whirl motion bifurcate into two whirl ratios, ~0.55 and ~0.45; until disappearing at a shaft speed of ~12.5 krpm. For lower shaft speeds, no major subsynchronous motions are observed.

Figure 29 shows waterfall plots of the rotor coastdown response for an imbalance displacement of u = 7.4 μm (out of phase). Figure 30 presents amplitudes of synchronous and subsynchronous components and whirl frequency ratios for this imbalance condition. A similar subsynchronous motion behavior than in the previous imbalance condition (see Figure 28) is evident, i.e. two subsynchronous motion regions with distinctive whirl frequency ratios.

In general, imbalance masses of increasing magnitude have a larger impact on the amplitudes of subsynchronous motion. Also, the speed range with more subsynchronous motion activity occurs near twice the system critical speeds, i.e. ~16.4 krpm and ~18 krpm. The rotordynamic performance of the test foil bearings show similar results as in other experimental programs reported in the literature, see Table 1. Typically, rotors supported on gas foil bearings show instabilities with whirl frequencies coinciding with the system natural frequencies. Figure 31 shows the subsynchronous amplitudes versus their corresponding whirl frequencies for the

maximum imbalance magnitudes of each test. The most severe (largest amplitudes of motion) occur at whirl frequencies $\omega_l = 120$ Hz (7,200 rpm) and $\omega_2 = 150$ Hz (9,000 rpm).
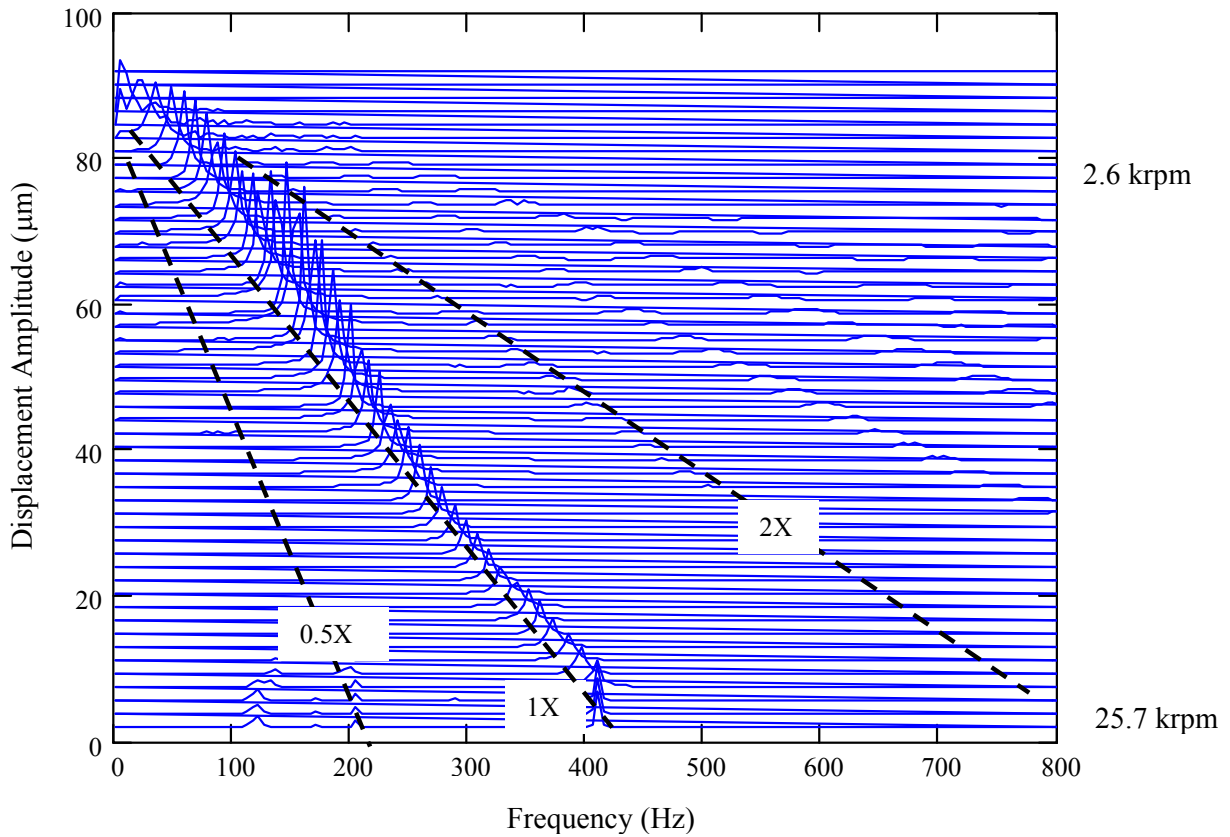

Figure 25 Waterfall plot of coastdown response for imbalance displacement u = 7.4 μm (in phase, Test A1). Air pressure at 34.4 kPa [5 psig] and measurements at rotor free end, vertical plane (Y_{FE})

Figure 26 Filtered components of synchronous and subsynchronous vibrations and whirl frequency ratio for imbalance displacement u = 7.4 μm (in phase, Test A1). Air pressure at 34.4 kPa [5 psig] and measurements at rotor free end, vertical plane (Y_{FE})
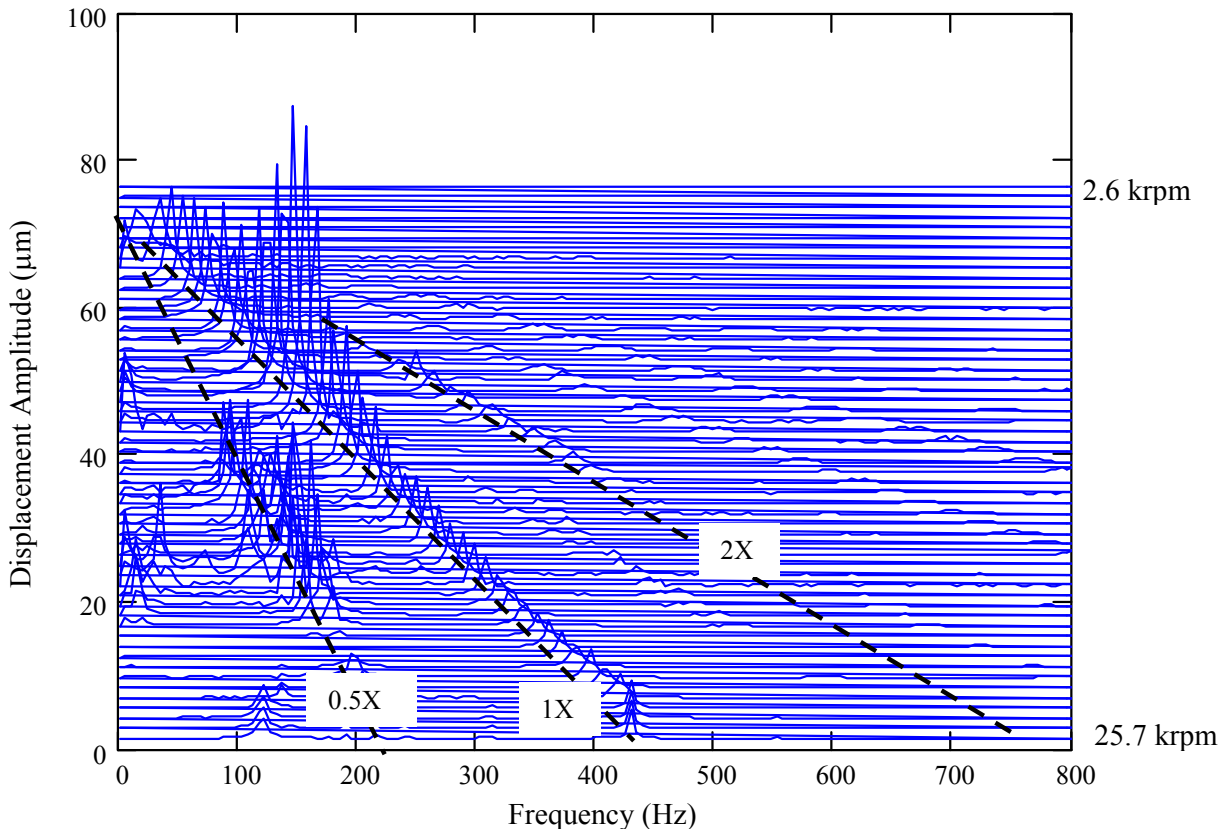
Figure 27 Waterfall plot of coastdown response for imbalance displacement *u* = 10.5 μm (in phase, Test A3). Air pressure at 34.4 kPa [5 psig] and measurements at rotor free end, vertical plane (*Y$_{FE}$*)
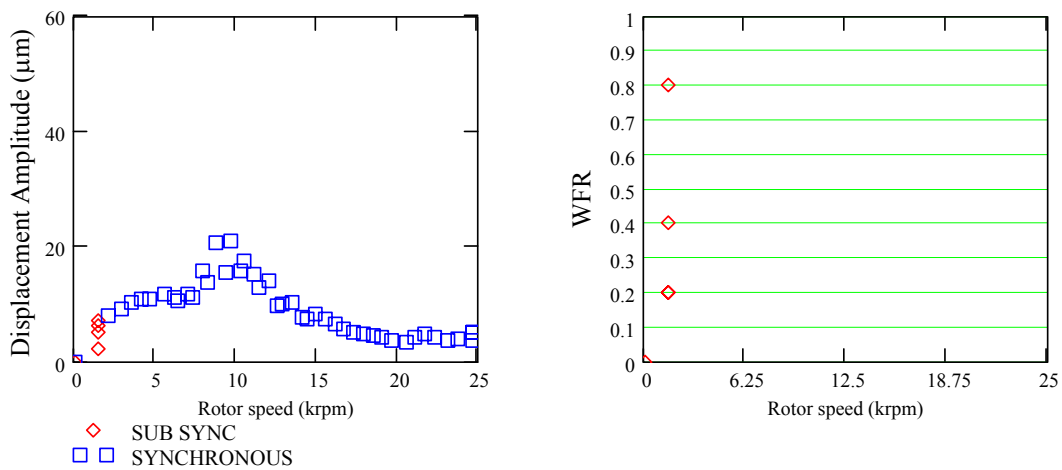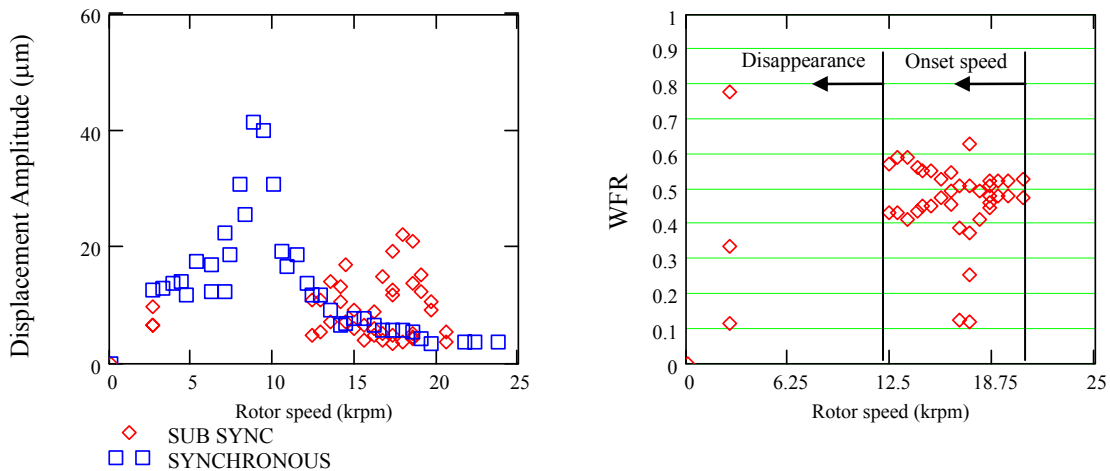

Figure 28 Filtered components of synchronous and subsynchronous vibrations and whirl frequency ratio for imbalance displacement *u* = 10.5 μm (in phase, Test A3). Air pressure at 34.4 kPa [5 psig] and measurements at rotor free end, vertical plane (*Y$_{FE}$*)

Figure 29 Waterfall plot of coastdown response for imbalance displacement _u_ = 7.4 μm (out of phase, Test B2). Air pressure at 34.4 kPa [5 psig] and measurements at rotor free end, vertical plane (Y_{FE})

Figure 30 Filtered components of synchronous and subsynchronous vibrations and whirl frequency ratio for imbalance displacement _u_ = 7.4 μm (out of phase, Test B2). Air pressure at 34.4 kPa [5 psig] and measurements at rotor free end, vertical plane (Y_{FE})
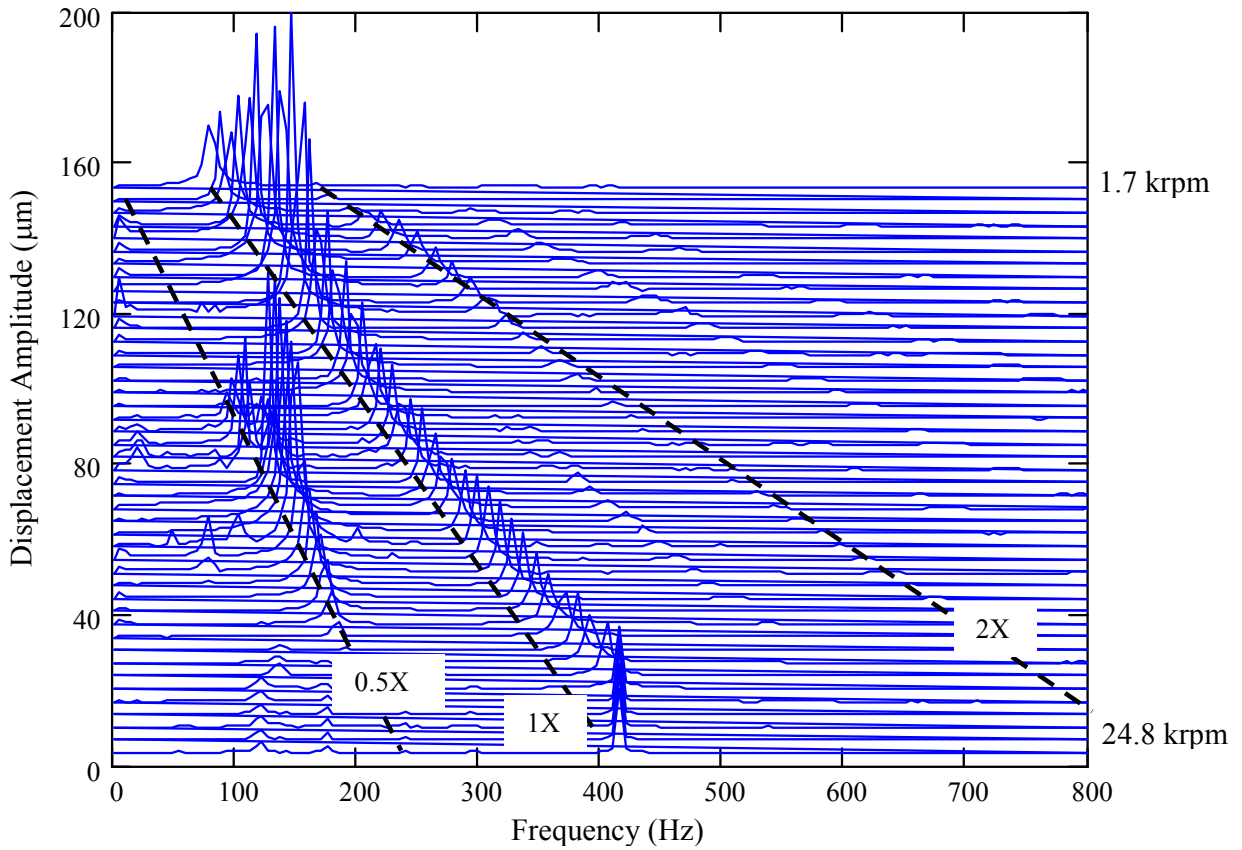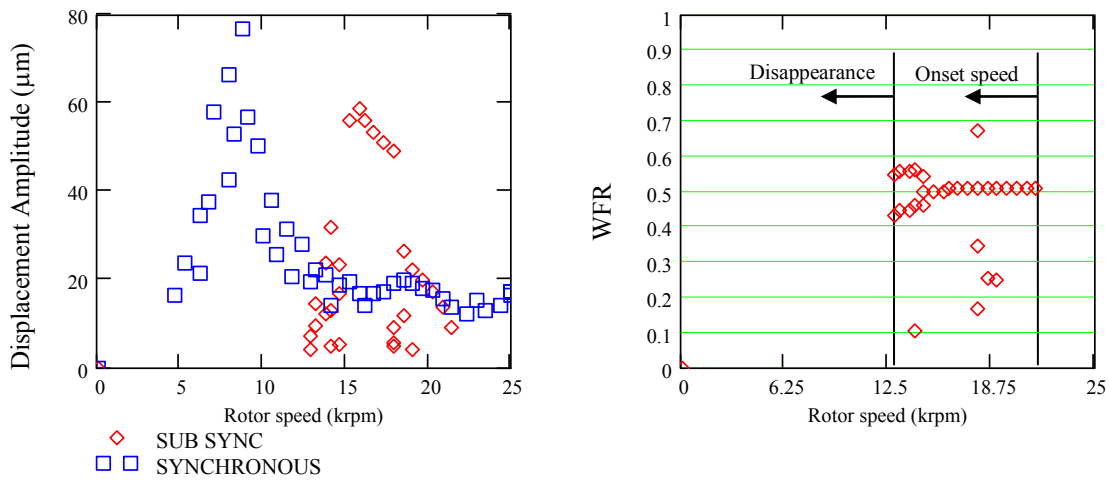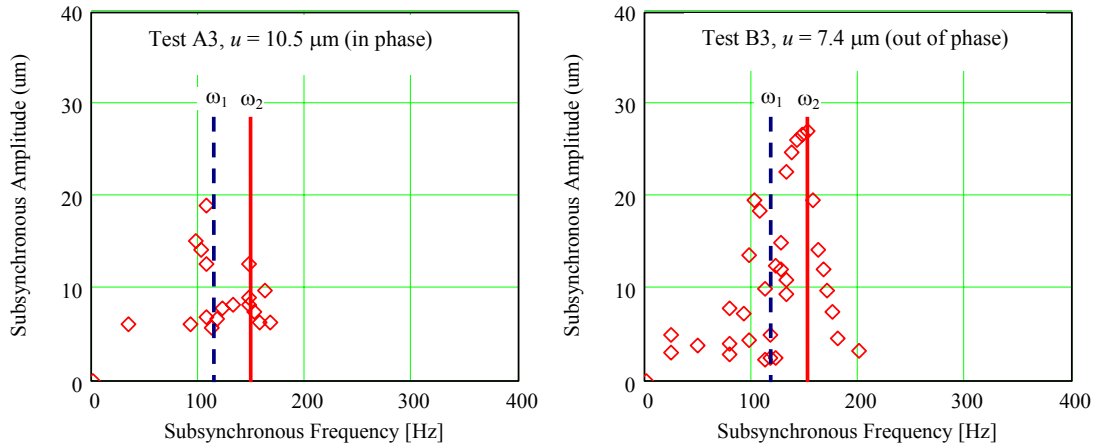
Figure 31 Subsynchronous amplitudes and frequencies of occurrence for imbalance *u* = 10.5 μm (in phase) and *u* = 7.4 μm (out of phase)

VII.   ROTOR MOTION ORBITS AT VARIOUS SHAFT SPEEDS

Motions orbits of the test rotor are obtained from the time varying displacement signals (vertical and horizontal) at selected shaft speeds. Figure 32 show synchronous filtered and direct motion orbits, at the rotor drive and free ends, for rotor speeds equal to 3.8 krpm; 8.2 krpm, and 16.7 krpm. The data corresponds to the largest *in-phase* imbalance, i.e. *u* = 10.5 μm. Figure 33 depict also orbital motions for the largest *out-of-phase* imbalance, i.e. *u* = 7.4 μm, at 4.7 krpm; 9.1 krpm, and 16.4 krpm

Figure 32B and Figure 33B display rotor orbits at the critical speeds, 8.2 krpm and 9.1 krpm, corresponding to the in phase and out of phase imbalances. The synchronous orbits at both rotor ends are clearly out of phase indicating the occurrence of a conical mode shape. The angle of the major axis of the elliptical orbit is about 45º from the horizontal plane, i.e. coinciding with the direction of the spot-weld for the top foil. Appendix D shows rotor orbits estimated at the bearing locations. Figure D1 and D2 show amplitudes of motion exceeding the estimated bearing clearances (44.6 μm and 34.0 μm for the free end and drive end bearings, respectively) for both imbalance tests.

Figure 32C and Figure 33C show rotor motion orbits at shaft speeds around twice the critical speed (~16 krpm). The rotor response contains large amplitude subsynchronous components with a whirl ratio of nearly 50% shaft speed. Again, the elliptical orbits appear to align with the spot weld location, in particular for the *in-phase* imbalance test.

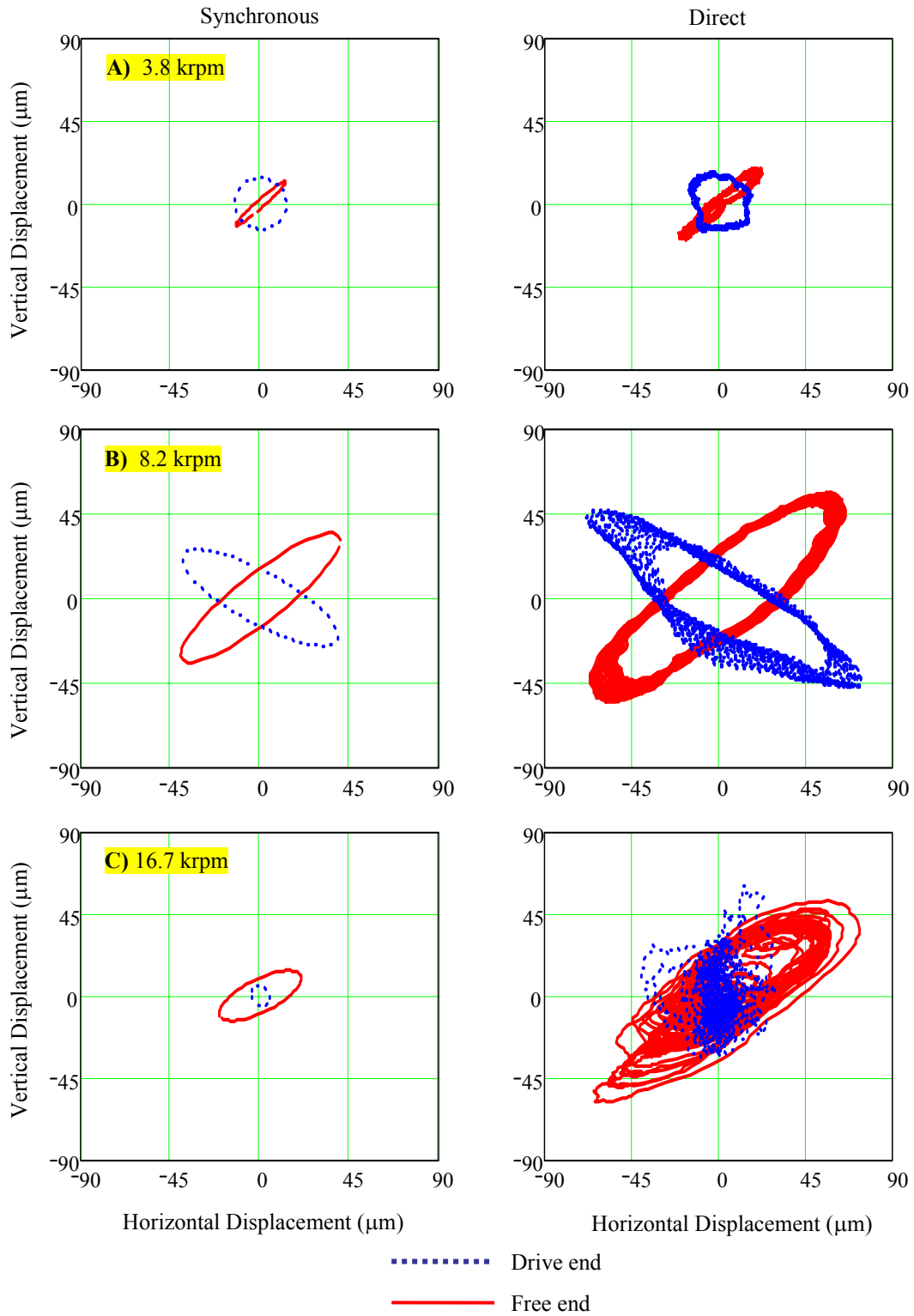**Figure 32 Synchronous and direct motion orbits at the drive and free rotor ends for an imbalance *u* = 10.5 μm (in phase). A) Rotor speed 3.8 krpm, B) 8.2 krpm and C) 16.7 krpm**

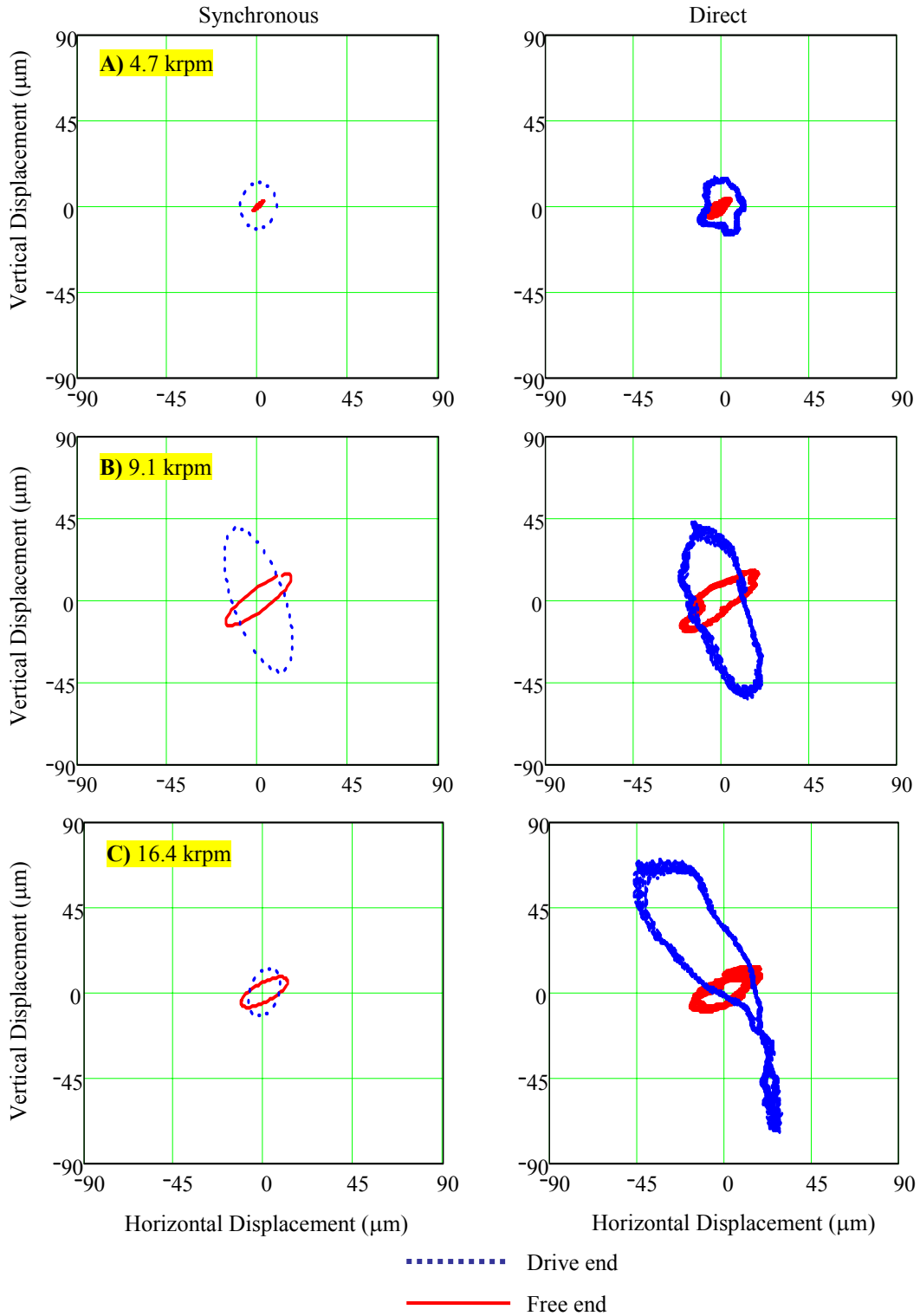**Figure 33 Synchronous and direct motion orbits at the drive and free rotor ends for an imbalance u = 7.4 μm (out of phase). A) Rotor speed 4.7 krpm, B) 9.1 krpm and C) 16.4 krpm**

VIII. EFFECT OF AIR PRESSURIZATION ON IMBALANCE RESPONSE AND SYSTEM STABILITY

This section presents experimental results of the influence of supply pressure on the rotor imbalance response and the system stability. Recall that the air supply inlet is at the test rig casing middle plane and exits axially through the test foil bearings. In these tests, the electromagnet was removed and a Plexiglas casing sealed the middle of the rig casing holding the bearings.

Constant speed tests for five air pressures equal to 40 kPa [6 psig], 136 kPa [20 psig], 204 kPa [30 psig], 272 kPa [40 psig] and 340 kPa [50 psig] followed. The test rotor imbalance is $u =$ 4.7 μm (*in phase* condition).

Figure 34 and Figure 35 show, for increasing supply pressure, the amplitudes of synchronous motions at shaft speeds coinciding with the system critical speed and twice its value. The supply pressure evidently ameliorates the synchronous amplitude at the critical speed. Changes in feed pressure barely affect the synchronous amplitude at the higher shaft speed, as seen Figure 35.
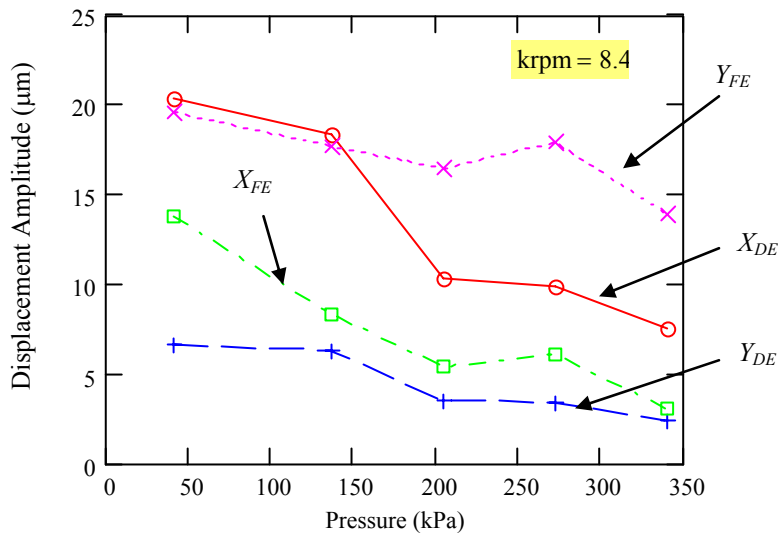

Figure 34 Synchronous vibrations at 8.4 krpm for increasing air supply pressures. Measurements taken at the four eddy current sensors
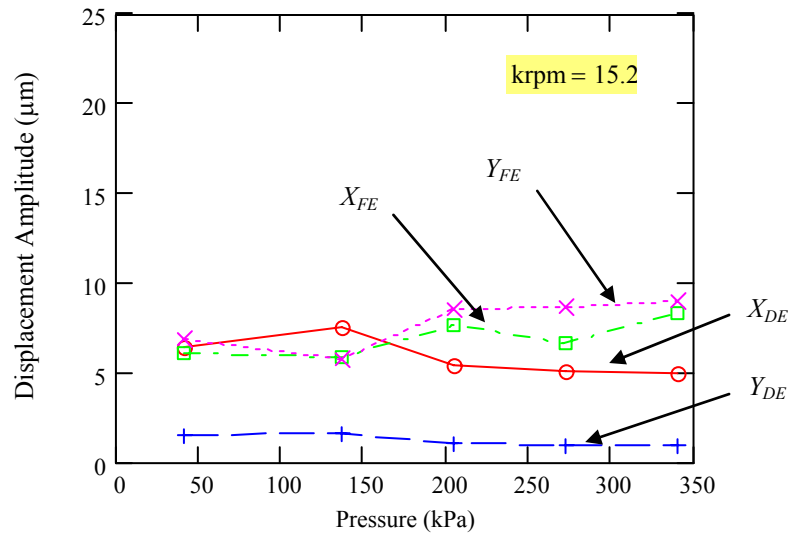
Figure 35 Synchronous vibrations at 15.2 krpm for increasing air supply pressures. Measurements taken at the four eddy current sensors

Air pressurization acts to reduce the rotor motion amplitude at the critical speeds, thus denoting an increase of damping at the foil bearings. The enhanced damping may arise from a "hovering" effect of the air flowing underneath the bearing top foil, as depicted in Figure 36. A very thin film of gas "lubricates" the contact regions allowing the bumps to slide over the bearing surface, thus dissipating more energy. No changes were noted in the system critical speed when increasing the supply pressure, thus discarding a *Lomakin* type effect. Experiments without rotor spinning further demonstrate that air pressurization does not load the foil or bumps since the rotor static position did not change.
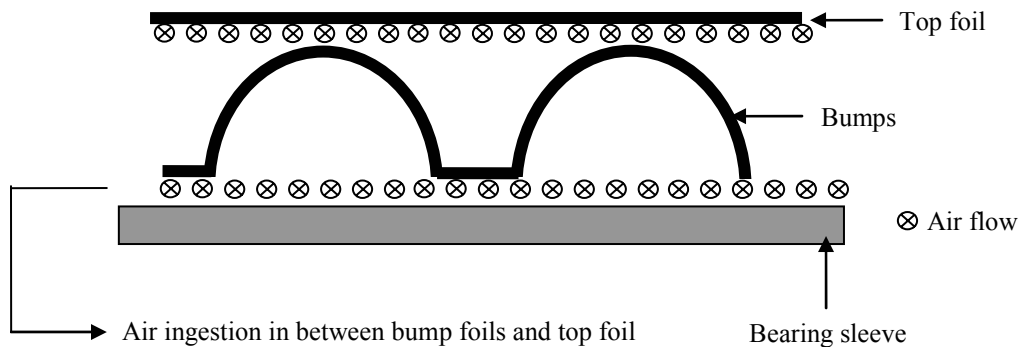
Figure 36 Schematic representation of air axial flow through test foil bearings

The effect of air supply pressure on the rotor/bearing stability was also evaluated for operation at a constant shaft speed (15.2 krpm), ~ twice the system critical speed. Figure 37 and Figure 38 display FFTs of rotor motion (drive end, horizontal and vertical planes) for three increasing supply pressures. The figures evidence a notable reduction in subsynchronous motion amplitudes when increasing the air feed pressure. For the highest supply pressure (50 psig), the main subsynchronous frequency, WFR~0.5, splits or bifurcates into two other frequencies, below and above the original value. The spectra for the highest feed pressures are rather broad, indicating a more "rugged" subsynchronous motion, albeit with less amplitude.

Figure 37 FFTs of steady state time responses at 15,200 rpm for three increasing air supply pressures; 40.8 kPa, 204 kPa and 340 kPa. Measurements taken at the drive end, horizontal direction (X_{DE})

Figure 38 FFTs of steady state time responses at 15,200 rpm for three increasing air supply pressures; 40.8 kPa, 204 kPa and 340 kPa. Measurements taken at the drive end, vertical direction (Y_{DE})
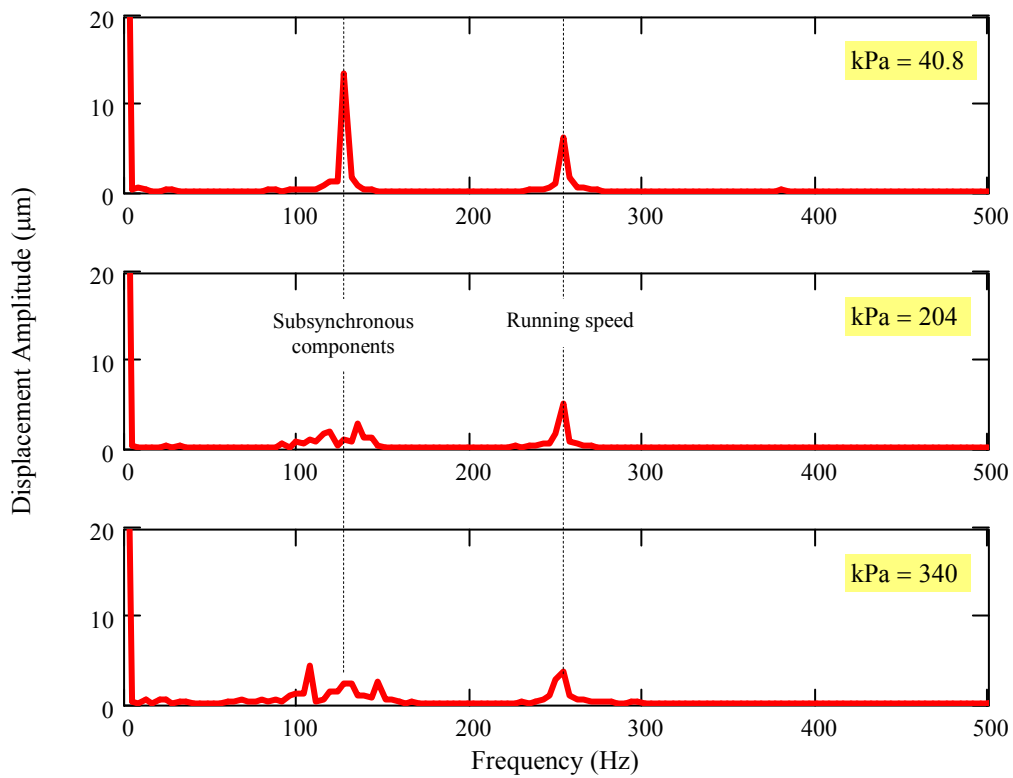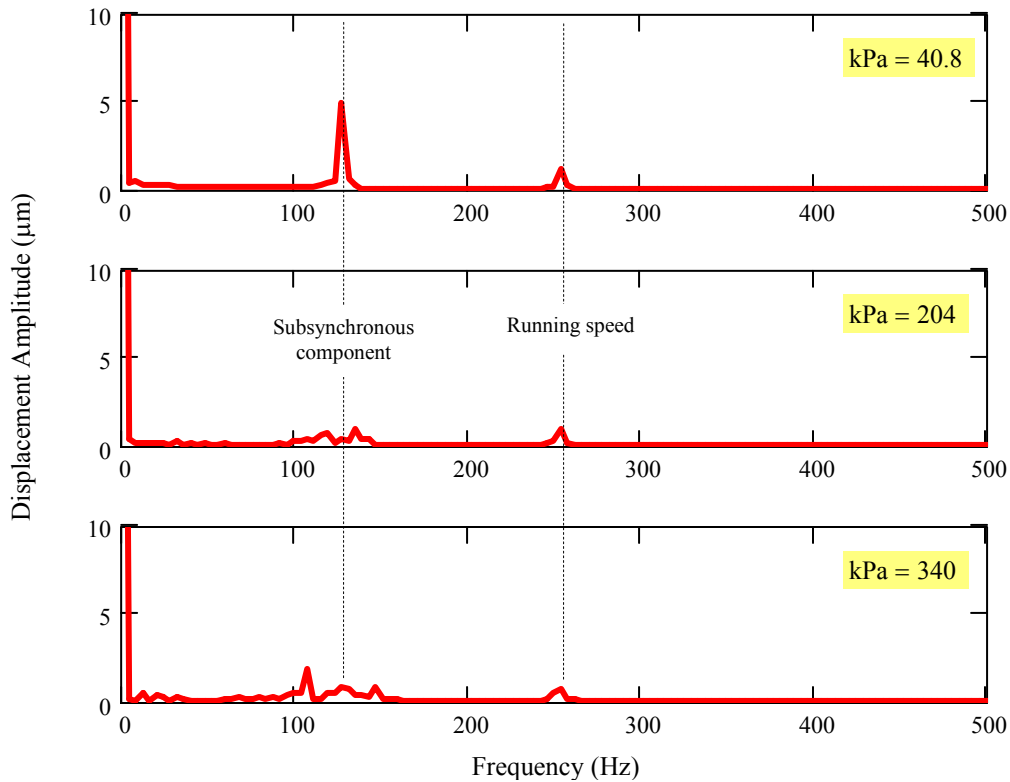
IX. TIME FOR ROTOR TO COASTDOWN

Finally, Figure 39 presents coastdown tests of rotor speed versus time for increasing air feed pressures. The imbalance condition corresponds to baseline. No major differences in the coastdown speed are noticeable when increasing the air pressure. However, two distinctive regions of exponential and linear decay are distinctive. An exponential approximation to the speed versus time curve, from 25,000 rpm to approximately 7,000 rpm, renders a goodness of correlation of 99.5%. Similarly, a linear approximation from 5,000 rpm to the minimum speed (~ 1,500 rpm) leads to a goodness of correlation of 99.6%. Thus, in the first region, the bearing drag is of viscous-type, while in the second region Coulomb-type (dry friction) from the contact between the journal and the foil dominates the bearing drag. In the transition region, the foil bearing touchdown speed occurs, as depicted in Figure 39. In general, the time constant is rather small, indicating large viscous dissipation effects due to minute operating clearances. One must

also realize that the drive DC motor remains coupled to the test rotor. Thus, the time constant represents that of the rotor and motor combined.

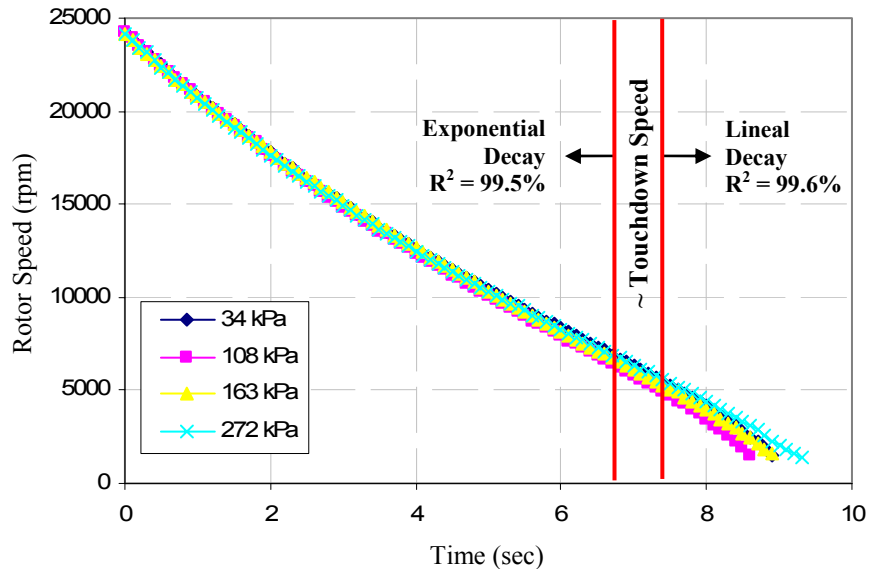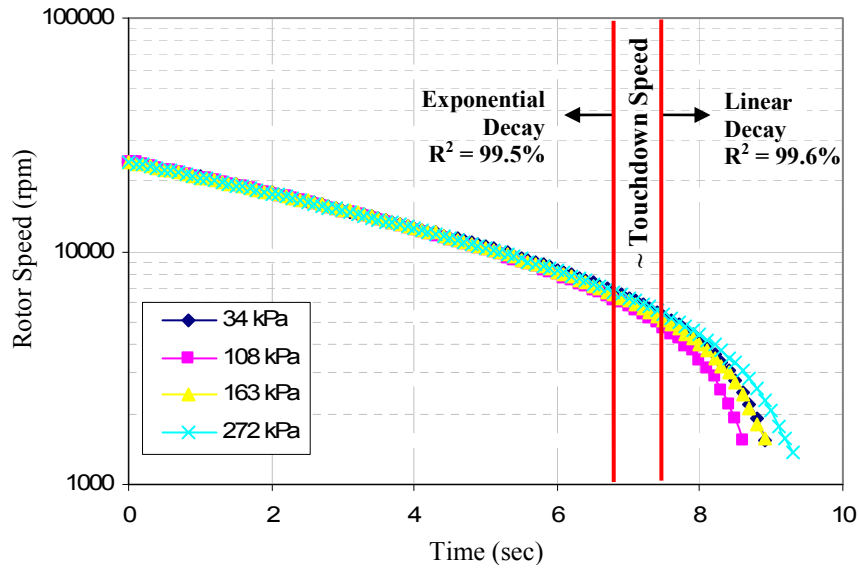**Figure 39 Coastdown speed versus time for rotor baseline condition and increasing air supply pressures. Linear scale**

Figure 40 Coastdown speed versus time for rotor baseline condition and increasing air feed pressures. Logarithmic scale

X. CONCLUSIONS

Coast down tests, conducted from a top speed of 25 krpm, aid to evaluate the rotordynamic performance of a hollow rotor, 0.98 kg [2.2 lb] weight, supported on gas foil bearings. In general, rotor synchronous responses at the critical speed appear nearly proportional to the added imbalance masses. Appearance of subsynchronous vibrations is sensitive to the level of imbalance added to the rotor, i.e. the larger the imbalance, the larger the magnitudes of subsynchronous motions. In general, subsynchronous frequencies track the shaft speed, being most severe at frequencies coinciding with the rotor rigid body mode natural frequencies. The whirl ratio at the onset of the instability equals 50% of shaft speed.

External air pressurization through the bearing ends aids to reduce the amplitude of synchronous motions while crossing a critical speed. Feed pressure has no discernable effect for synchronous motions well above the critical speed. The air-film lubricates the contact regions allowing the bumps to hover easily, thus dissipating more energy. Importantly enough, the tests also demonstrate that increasing air pressures ameliorates the amplitudes of sub synchronous motions.

The experimental investigation aids to understand the rotordynamic performance of gas foil bearings. There are commercial claims stating foil bearings are free of rotordynamic instabilities. The present experimental results, however, show that rotor subsynchronous motions are of large amplitude though confined over a well defined rotor speed range which includes twice the system critical speed. Operation free of subsynchronous motion may be possible at even higher shaft speeds. This assertion may be corroborated in future tests with a faster drive motor. Also, planned tests will include activating the electromagnetic loader to establish the influence of applied static loads on the rotor-bearing system response and stability.

Identification of synchronous (linearized) force coefficients for the test gas foil bearings is under way. The recorded test data supports the modeling requirements to extract the force coefficients from the measured synchronous responses, in spite of the flagrant system instability.

REFERENCES

[1] Agrawal, G. L., 1997, "Foil Air/Gas Bearing Technology—An Overview," International Gas Turbine & Aeroengine Congress & Exhibition, Orlando, Florida, ASME paper 97-GT-347.

[2] Heshmat, H., Walowit, J., and Pinkus, O., 1983, "Analysis of Gas-Lubricated Compliant Journal Bearings," ASME Journal of Lubrication Technology, **105** (4), pp. 647-655.

[3] Peng, J.-P, and Carpino, M., 1993, "Calculation of Stiffness and Damping Coefficient for Elastically Supported Gas Foil Bearings," ASME Journal of Tribology, **115** (1), pp. 20-27.

[4] DellaCorte, C., and Valco, M., 2000, "Load Capacity Estimation of Foil Air Bearings for Oil-Free Turbomachinery Applications," STLE Tribology Transactions, **43** (4), pp. 795-801.

[5] Ku, C.-P, and Heshmat, H., 1992, "Complaint Foil Bearing Structural Stiffness Analysis Part I: Theoretical Model - Including Strip and Variable Bump Foil Geometry," ASME Journal of Tribology, **114** (2), pp. 394-400.

[6] Ku, C.-P, and Heshmat, H., 1993, "Complaint Foil Bearing Structural Stiffness Analysis Part II: Experimental Investigation," ASME Journal of Tribology, **113** (3), pp. 364-369.

[7] Iordanoff, I., 1999, "Analysis of an Aerodynamic Complaint Foil Thrust Bearing: Method for a Rapid Design," ASME Journal of Tribology, **121**, pp. 816-822.

[8] Rubio, D., and San Andrés, L., 2004, "Bump-Type Foil Bearing Structural Stiffness: Experiments and Predictions," ASME Paper GT 2004-53611.

[9] Ku, C.-P, and Heshmat, H., 1994, "Structural Stiffness and Coulomb Damping in Compliant Foil Journal Bearing: Theoretical Considerations," STLE Tribology Transactions, **37** (3), pp. 525-533.

[10] Ku, C.-P, and Heshmat, H., 1994, "Structural Stiffness and Coulomb Damping in Compliant Foil Journal Bearing: Parametric Studies," STLE Tribology Transactions, **37** (3), pp. 455-462.

[11] Heshmat, H., 1994, "Advancements in the performance of Aerodynamic Foil Journal Bearings: High Speed and Load Capability," ASME Journal of Tribology, **116** (2), pp. 287-295.

[12] DellaCorte, C., and Valco, M., 2003, "Oil-Free Turbomachinery Technology for Regional Jet, Rotorcraft and Supersonic Business Jet Propulsion Engines," American Institute of Aeronautics and Astronautics, ASABE 2003 – 1182.

[13] Gu, A., 1988, "Process Fluid Foil Bearing Liquid Hydrogen Turbopump," AIAA/ASME/SAE/ASEE 24th Joint Propulsion Conference, Paper No. AA-88-3130.

[14] Chen, H., Howarth, R., Geren, B., Theilacker, J., and Soyars, W., 2001, "Application of Foil Bearing to Helium Turbocompressor," Proceedings of the 30th Turbomachinery Symposium, pp. 103-112, Houston, TX.

[15] Ku, C-P., 1993, "An Experimental and Theoretical Study of the Dynamic Structural Stiffness in Compliant Foil Journal Bearings," ASME 14th Biennial Conference on Mechanical Vibration and Noise, Albuquerque, NM, DE-Vol. 63, *Vibration of Mechanical Systems and the History of Mechanical Design*, pp. 83-88.

[16] Heshmat, H., and Ku, C.-P., 1994, "Structural Damping of Self-Acting Compliant Foil Journal Bearings," ASME Journal of Tribology, **116** (1), pp. 76-82.

[17] Salehi, M., Heshmat, H., and Walton, J., 2003, "On the Frictional Damping Characterization of Compliant Bump Foils," Transactions of the ASME, **125** (4), pp. 804-813.

[18] Heshmat, H., 1994, "Advancements in the performance of Aerodynamic Foil Journal Bearings: High Speed and Load Capability," ASME Journal of Tribology, **116** (2), pp. 287-295.

[19] Heshmat, H., 2000, "Operation of Foil Bearing Beyond the Bending Critical Mode," ASME Journal of Tribology, **122** (1), pp. 192-198.

[20] Howard, S., DellaCorte, C., Valco, M.-J., Prahl, J.-M., and Heshmat, H., 2001, "Steady-State Stiffness of Foil Air Journal Bearings at Elevated Temperatures," STLE Tribology Transactions, **44** (3), pp. 489-493.

[21] J.F., Walton II, and H., Heshmat, 2002, "Application of Foil Bearings to Turbomachinery Including Vertical Operation," Transactions of ASME, **124**, pp. 1032-1041.

[22] E., Swason, J.F., Walton II, H., Heshmat, 2002, "A Test Stand for Dynamic Characterization of Oil-Free Bearings for Modern Gas Turbine Engines," Proceedings of the ASME Turbo Expo 2002, Amsterdam, The Netherlands.

[23] Lee, Y,B., Kim, T.H, Kim, C.H., and Lee, N.S., 2003, "Suppression of Subsynchronous Vibrations Due to Aerodynamic Response to Surge in a Two-Stage Centrifugal Compressor with Air Foil Bearings," STLE Presentation No. AM03-8.

[24] Y., Hou, L.Y., Xiong, and C.Z., Chen, 2004, "Experimental Study of a New Foil Air Bearing with Elastic Support," Tribology Transactions, **47**, pp. 308-311.

[25] DellaCorte, C., and Valco, M., 2000, "Load Capacity Estimation of Foil Air Journal Bearing for Oil-Free Turbomachinery Applications," STLE Tribology Transactions, **43** (4), pp. 795-801.

[26] Peng, J.-P, and Carpino, M., 1993, "Calculation of Stiffness and Damping Coefficient for Elastically Supported Gas Foil Bearings," ASME Journal of Tribology, **115** (1), pp. 20-27.

[27] San Andrés, L., 1994, "Turbulent Flow Foil Bearing for Cryogenic Applications," ASME Journal of Tribology, **117** (1), pp. 185-195.

[28] Lee, Y.-B., Kim, T.-H., Kim, C.-H., Lee, N.S., and Choi, D.-H., 2003, "Unbalance Response of a Super-Critical Rotor Supported by Foil Bearings – Comparison with Test Results," STLE Tribology Transactions, **47** (1), pp. 54-60.

[29] Lee, Y.-B., Kim, T.-H., Kim, C.-H., Lee, N.S., and Choi, D.-H., 2004. "Dynamic Characteristics of a Flexible Rotor System Supported by a Viscoelastic Foil Bearing (VEFB)," Tribology International, **37**, pp. 679-687.

[30] DellaCorte, C., Zaldana, A., and Radil, K., 2003, "A System Approach to the Solid Lubrication of Foil Air Bearing for Oil-Free Turbomachinery," ASME Journal of Tribology, **126** (1), pp. 200-207.

[31] Radil, K., Howard, S., and Dykas, B., 2002, "The Role of Radial Clearance on the Performance of Foil Air Bearings," STLE Tribology Transactions, **45** (4), pp. 485-490.

[32] Howard, S., DellaCorte, C., Valco, M.-J., Prahl, J.-M., and Heshmat, H., 2001, "Dynamic Stiffness and Damping Characteristics of a High-Temperature Air Foil Journal Bearing," STLE Tribology Transactions, **44** (4), pp. 657-663.

[33] Iordanoff, I., 1999, "Analysis of an Aerodynamic Complaint Foil Thrust Bearing: Method for a Rapid Design," ASME Journal of Tribology, **121**, pp.816-822.

APPENDIX A. IDENTIFICATION OF *FB* STRUCTURAL DYNAMIC COEFFICIENTS FROM RAP TESTS ON ROTOR

An experimental procedure was developed to estimate rigid body mode natural frequencies and to identify *FB* structural coefficients. The test procedure consisted of two different (linearly independent) impact excitations at the rotor center of gravity and rotor end. Figure A1 shows the time varying impact load and ensuing rotor displacements for the two set of impact locations, i.e. at the rotor center of gravity and the rotor motor end. The measured rotor displacements (z_A, z_B, y_A and y_B) are recorded at the both rotor ends (A and B) in the horizontal (y) and vertical (z) directions. Cross-coupled motions are found to be significantly small in comparison with direct rotor displacement, i.e. approximately 7% of direct motions. Figure A2 shows the Fast Fourier Transform of the calculated rotor motion at the center of gravity (z_G) and the rotor angular displacement (θ). Amplitudes of vibration at the center of gravity for each impact excitation indicate that the first and second rigid body mode natural frequencies are approximately 156 Hz and 164 Hz, respectively.

A comprehensive parameter identification procedure to identify *FB* structural stiffness and equivalent damping coefficients was developed. The rotor/foil bearing system was modeled as 2-degree of freedom linear mechanical system. Structural stiffness and damping coefficients are estimated by calculating the experimental dynamic stiffness matrix from the test data in the frequency domain. Figure A3 shows that an increase in the excitation frequency slightly increases the direct stiffness coefficients (K_{zz}) and decreases the direct damping coefficients (C_{zz}) for both test foil bearings. The structural stiffness of the foil bearing located at the free end is slightly larger than the foil bearing located at the motor end, while equivalent viscous damping coefficients are slightly larger on the *FB* located at the motor end than the one located at the free end.
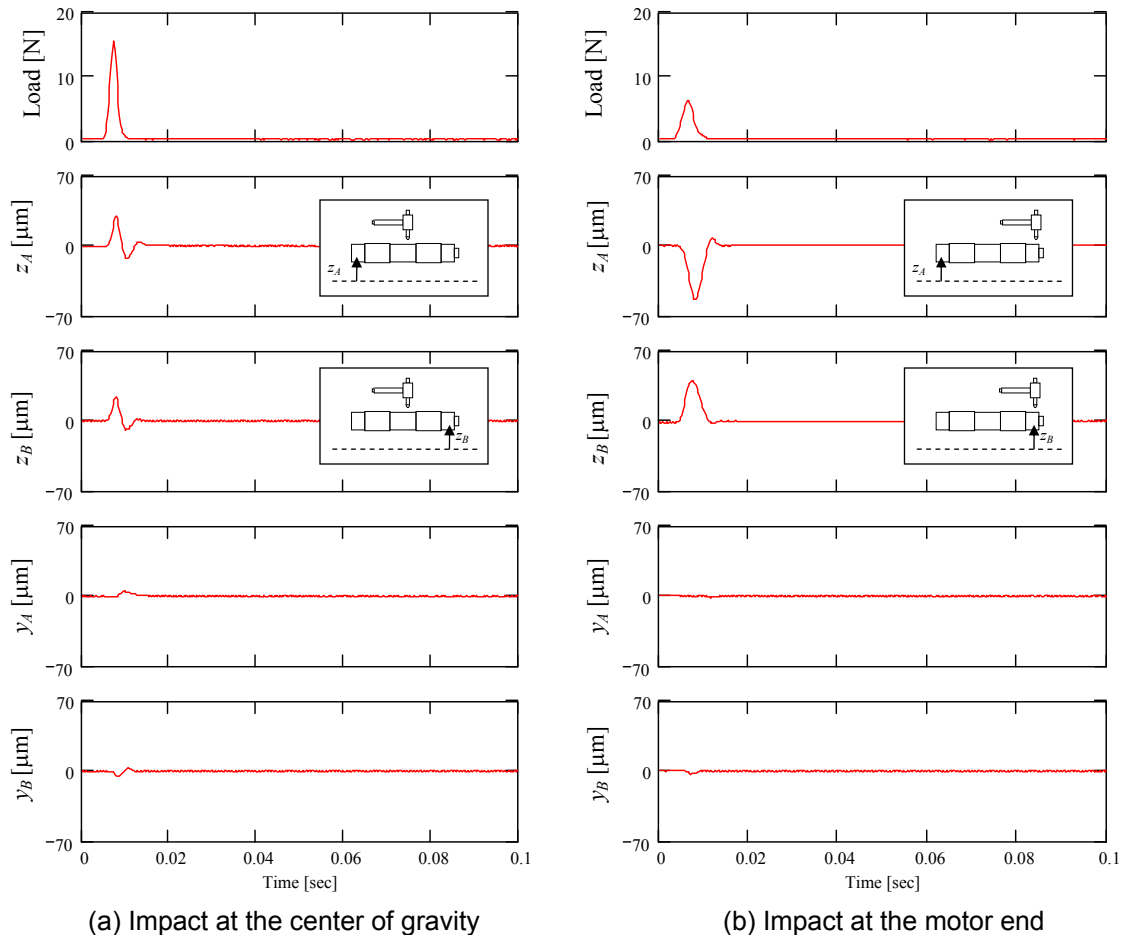
(a) Impact at the center of gravity

(b) Impact at the motor end

Figure A1 Time dependant impact force and rotor displacements for load excitations at the a) center of gravity and b) the motor end

A) Amplitudes of vertical displacements at the center of gravity
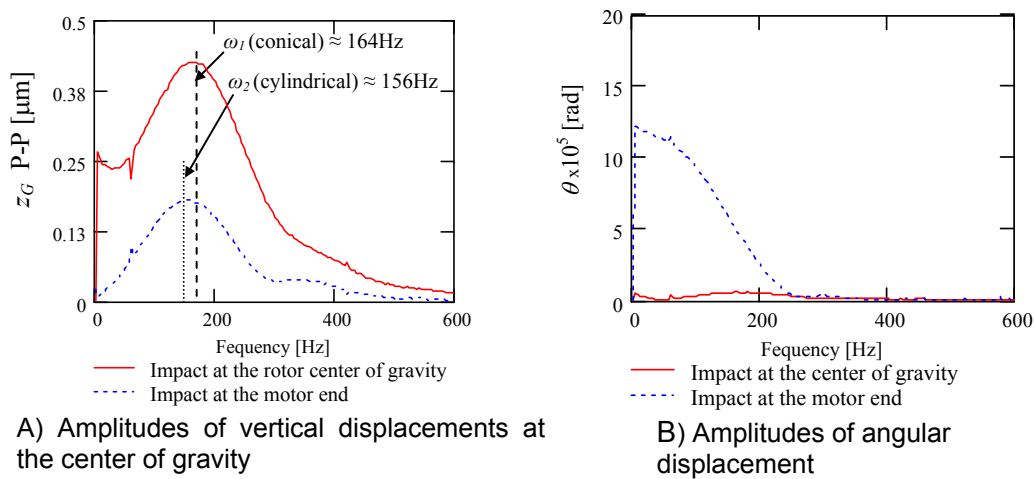
B) Amplitudes of angular displacement

Figure A2 Impact forces, a) at the rotor center of gravity and b) at the motor end, and calculated c) rotor center of gravity displacement and d) angular deflections varying with frequencies
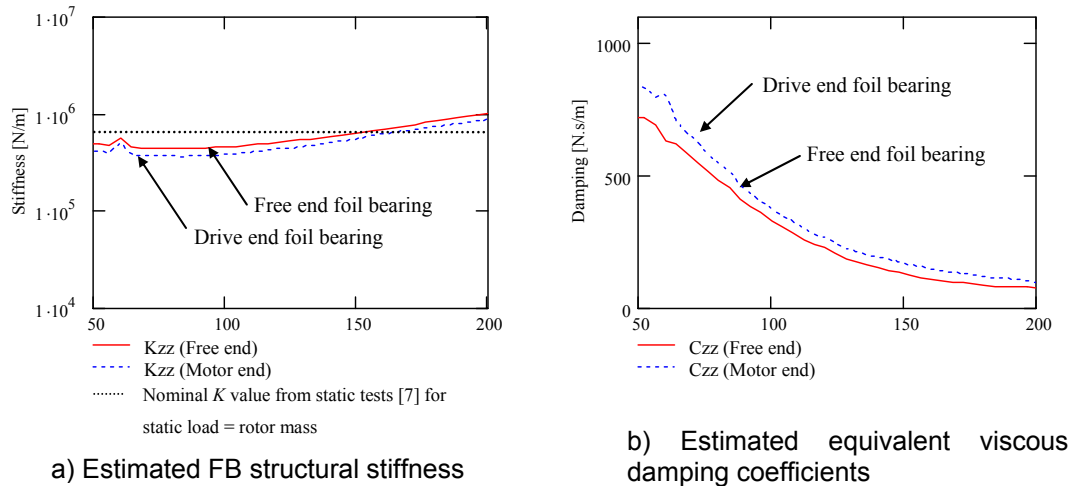
a) Estimated FB structural stiffness

b) Estimated equivalent viscous damping coefficients

Figure A3 Identified stiffness and damping coefficients versus frequency

The logarithmic decrement method is used to assess modal damping ratios for the test foil bearings. Linear and exponential approximations of the rotor transient responses allow determining dry friction coefficients and modal damping ratios of the test foil bearings. Table A1 shows experimental results of modal damping ratios for both foil bearings. Notice the large damping ratio coefficients for both bearing for non-rotating operations.

Table A1 Identified *FB* parameters from linear and exponential curve fit of rotor transient response

Identified FB parameters	Symbol	FB Drive end	FB Free end
Dry Friction Force, N	F_{DRY}	2.2	3.8
Dry friction coefficient	μ	0.15	0.24
Average structural Stiffness, MN/m	K	0.8	0.9
Standard deviation of K, MN/m	K_S	0.18	0.19
Modal damping ratio	ζ	**42%**	**35%**

APPENDIX B. ELECTROMAGNETIC LOAD ACTUATOR DESCRIPTION

For identification of *FB* force coefficients, an electromagnetic load fixture delivers non-contacting magnetic forces to the rotor middle span while the rotor spins. The electromagnetic loads are generated through a series of copper wires wounded around a high-magnetic permeability material made of Alloy-49. The electromagnetic forces are transmitted through small air gaps, typically varying from 0.25mm [0.010 in] to 0.50 mm [0.020 in], between the electromagnet tip and the rotor surface. Increasing current magnitudes through the copper wires boost electromagnetic forces applied to the rotor until reaching the electromagnet saturation zone. Figure A1 depicts a close view of the electromagnetic load actuator. Table B1 outlines the electromagnet material properties as well as its major dimensional features.
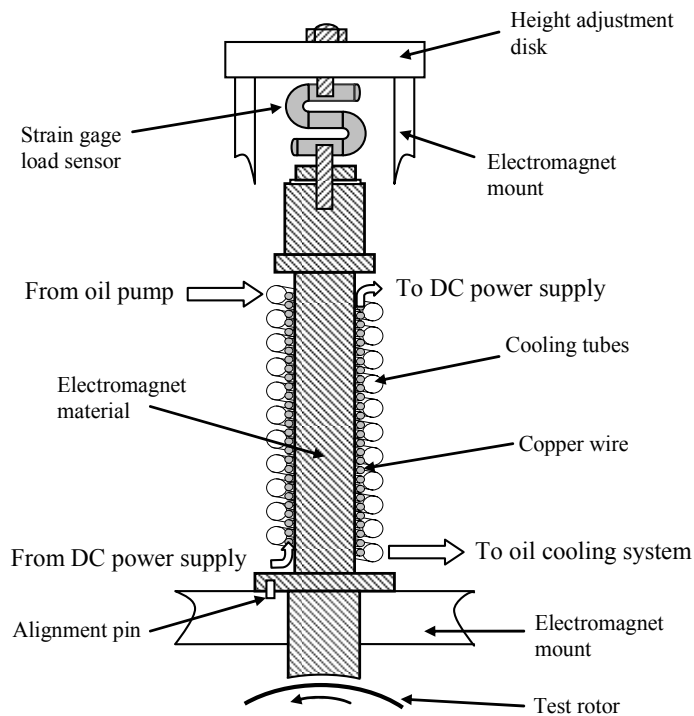

Figure B1 Schematic view of the electromagnetic actuator installed on the *FB* test rig

The electromagnetic load actuator exerts attracting forces to the test rotor, which also react to the strain gage load sensor. The opposite end of the strain gage features a disk mechanism upon which the electromagnetic-rotor gap is adjusted. Upon installation, special care is taken to ensure that the electromagnet aligns properly with the rotor in order to avoid rubs while rotor spinning.

Therefore, an alignment pin prevents the electromagnet to swivel along its axial axis. A cooling system with lubricant flowing through cooper piping wounded around the magnet conduct heat away. Oil flows from a cooling reservoir tank that keeps the oil temperature at approximately 25 ºC. The oil contained on the cooling reservoir is brought to the electromagnet using a centrifugal pump of variable speed.

A DC power source supplies variable output voltages (0-25V) and currents (0-80A) to the cooper wires wounded on the electromagnet. In addition, a strain gage load sensor records the electromagnetic force applied to the test rotor, while a strain gage panel meter displays the applied electromagnetic force. To verify a proper temperature isolation of the electromagnet surface, a K-type thermocouple records the surface temperature at the copper wires when re-circulated cool oil flows through the tubes.

**Table B1 Electromagnet material properties, physical dimensions and main characteristics**

Material Properties	SI Units	English Units
Material	Steel Alloy-49	
Material density, ρ_E	8166 kg/m^3	0.294 lb/in^3
Modulus of elasticity, E_E	51.7 MPa	7498.5 Psi
Saturation flux density, ρ_{SAT}	1.5000 Tesla	15000 Gauss
Maximum permeability[14], μ_o	103000	
Physical Dimensions		
Pole area, A_P	451.61 mm^2	0.70 in^2
Tip arcuate diameter, D_E	35.05 mm	1.38 in
Length of wounded wire, L_E	101.6 mm	4.00 in
Number of turns, N_T	~ 420	

---

[14] Maximum permeability after being hydrogen annealed.

APPENDIX C. WATERFALL PLOTS OF BASELINE ROTOR RESPONSE AT THE FREE END, HORIZONTAL AND VERTICAL DIRECTIONS
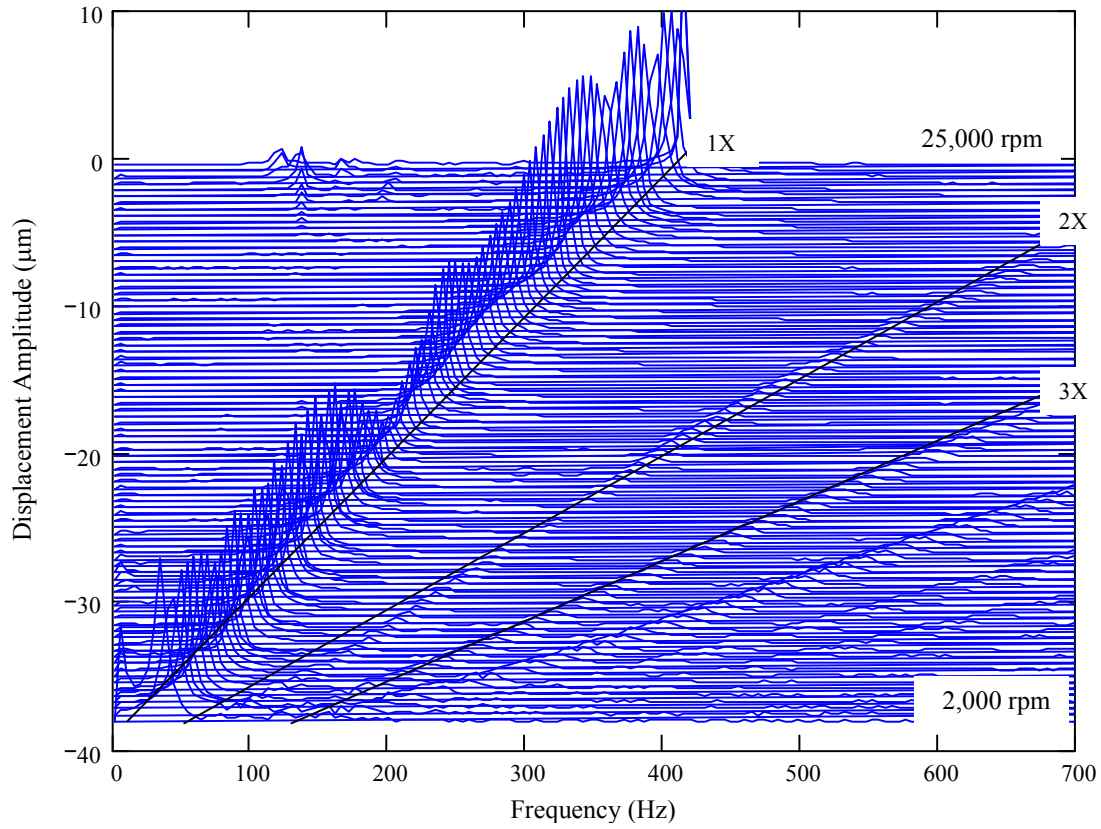
Figure C1 Waterfall plot of baseline rotor response at free end, vertical location (X_{FE}). Air pressure at 34.4 kPa [5 psig]
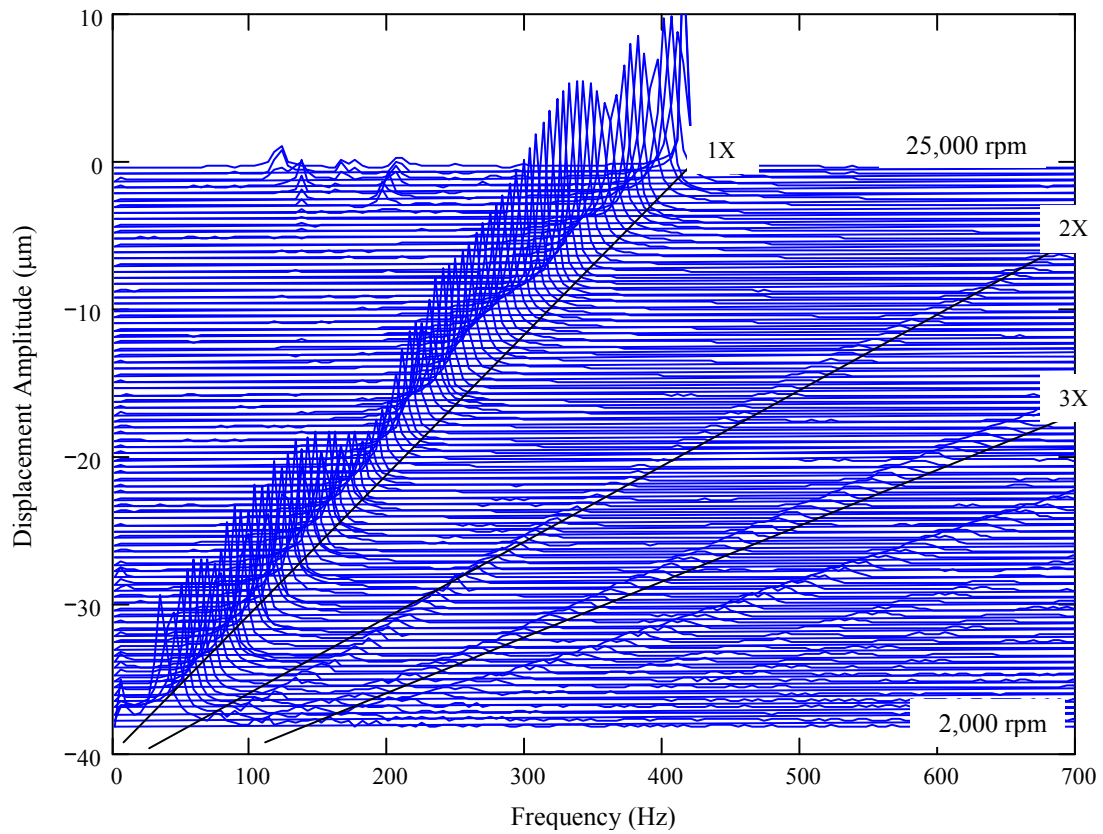
Figure C2 Waterfall plot of baseline rotor response at the free end, vertical location (Y_{FE}). Air pressure at 34.4 kPa [5 psig]

APPENDIX D. IMBALANCE RESPONSE AT THE BEARING CENTER LOCATION

A simple geometrical transformation assuming rigid rotor motions determines the rotor imbalance response at the bearing center locations, as shown in Figures B1 and B2 for imbalance tests A. The calculations show large motions that may exceed the bearings nominal clearances.
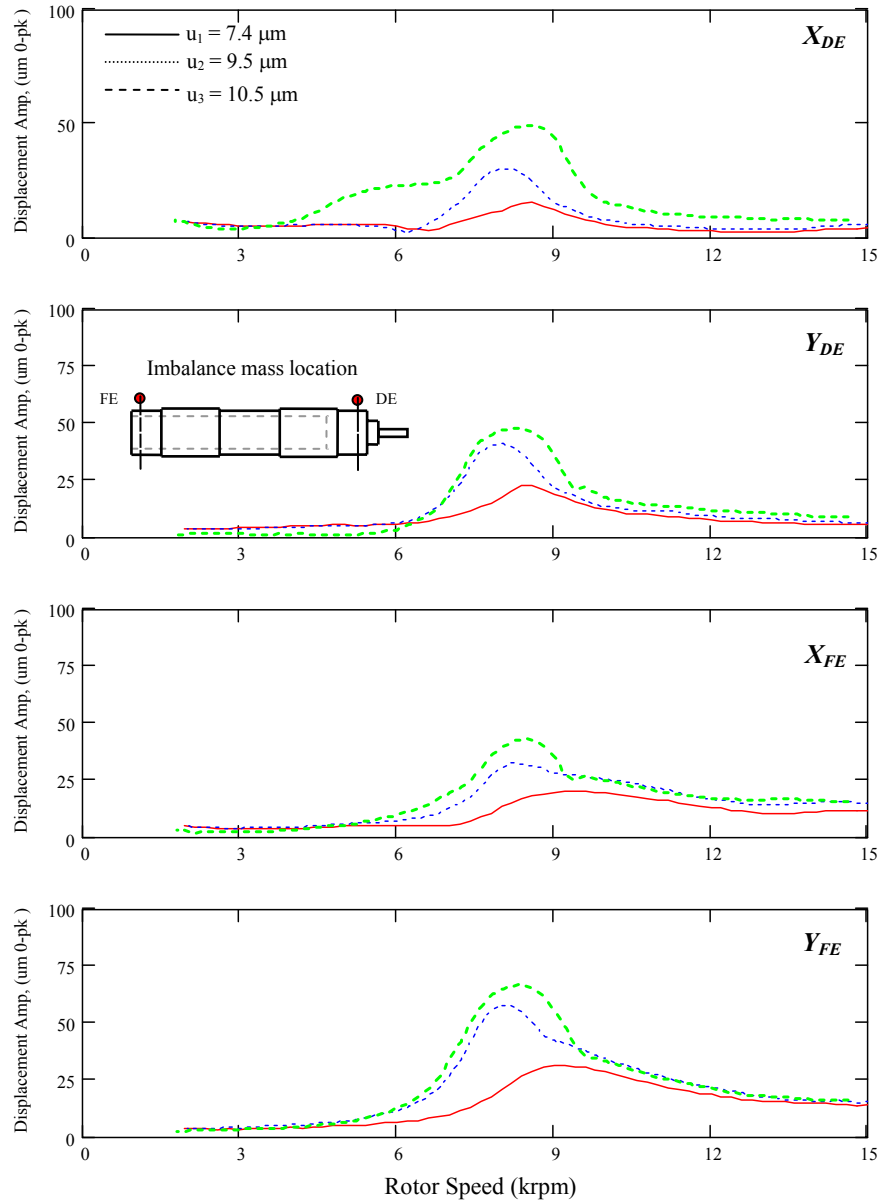
Figure D1 Calculated synchronous rotor response at the bearing <u>center locations</u> for imbalance tests A and air pressure at 34.4 kPa [5 psig]. Estimated clearances c = 22.3 μm and 17.0 μm at the drive and free ends.
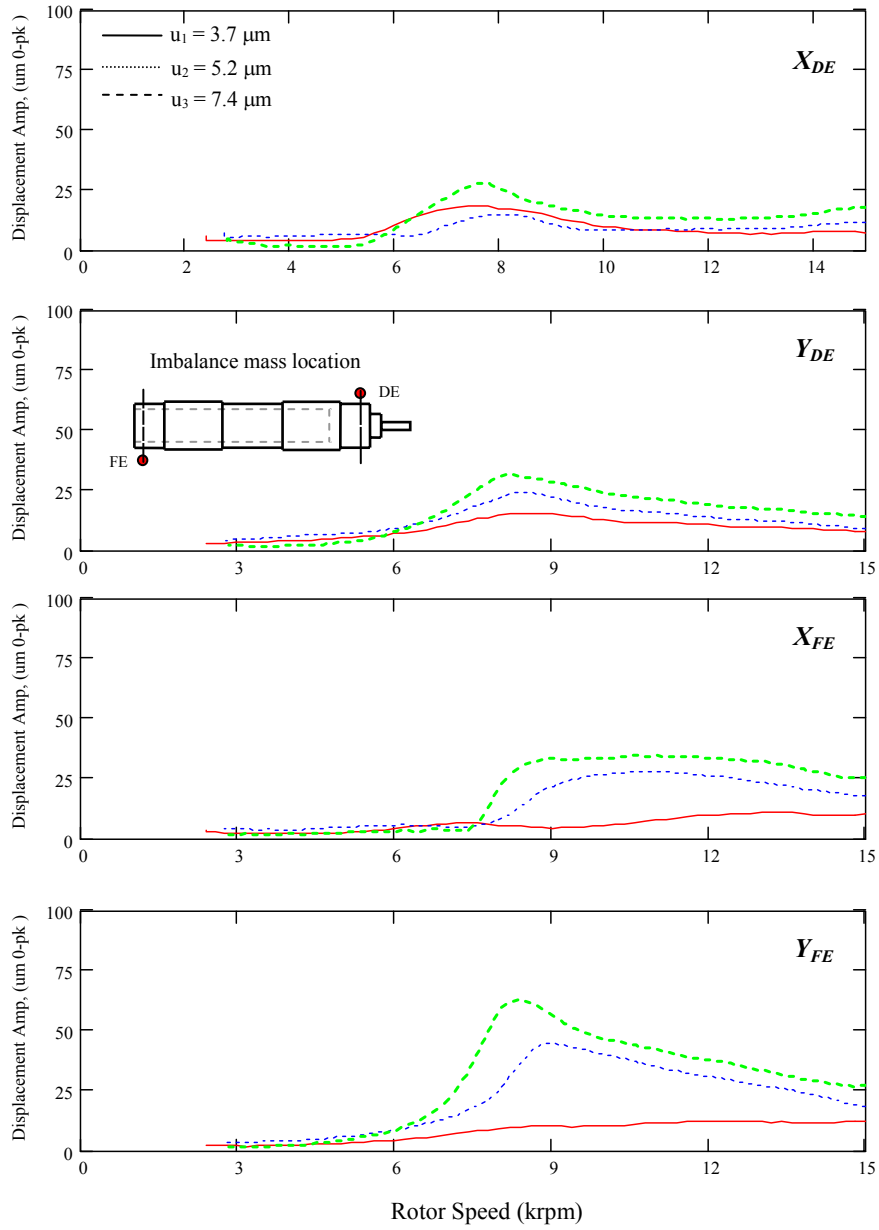
Figure D2 Calculated synchronous rotor response at the bearing <u>center locations</u> for imbalance tests B and air pressure at 34.4 kPa [5 psig]. Estimated clearances *c* = 22.3 μm and 17.0 μm at the drive and free ends.

APPENDIX E. ROTOR/BEARING SYSTEM LINEARITY

A simple verification of the system linearity is conducted for the test synchronous responses. In a linear system, the amplitude of the synchronous response is proportional to the imbalance magnitude, u. Figure E1 shows the recorded synchronous amplitude responses multiplied by $(u_j/u_1)_{j=1,2,3}$, where the lowest imbalance u_1, in and out of phase, is taken as a basis. In general, the synchronous amplitudes for each of the three tests coincide for shaft speeds away from the critical speeds. The results evidence that, in spite of the severe subsynchronous motions recorded at high shaft speeds, the rotor motions synchronous with shaft speed are similar, and more importantly, **predictable**! Hence, identification of synchronous force coefficients for the test foil bearings should be quite reliable.
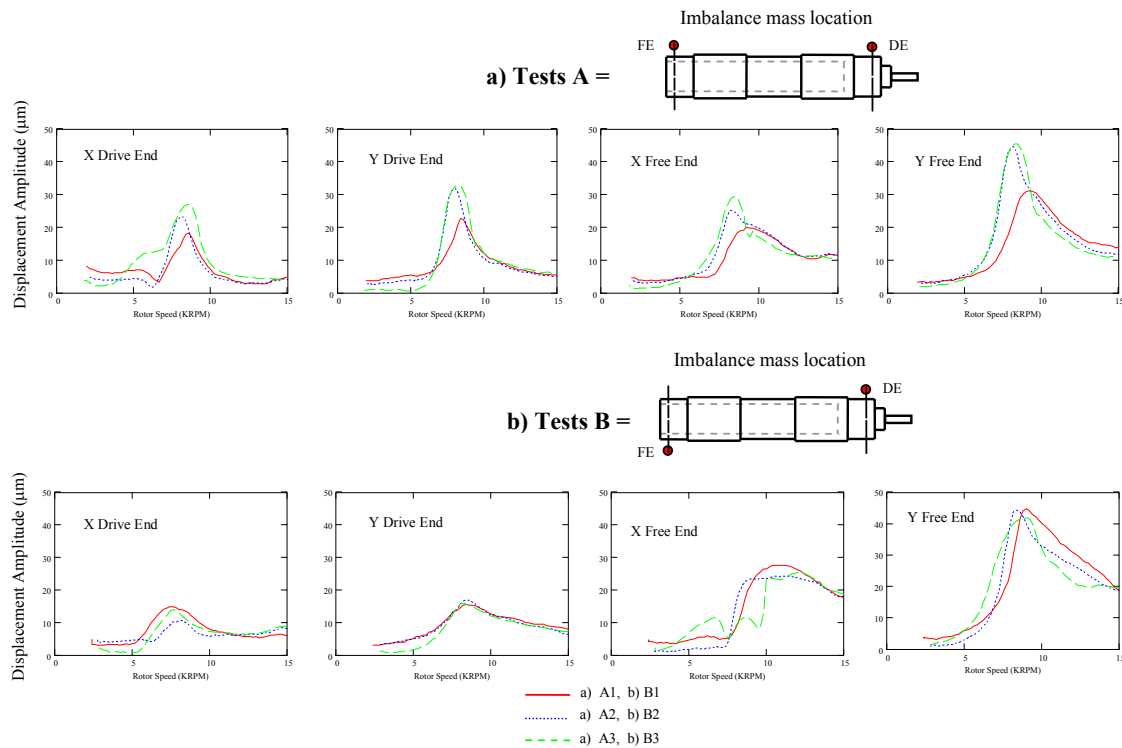

Figure E 1 Verification of rotor/bearing system linearity from synchronous response for a) imbalance tests A; and b) imbalance tests B

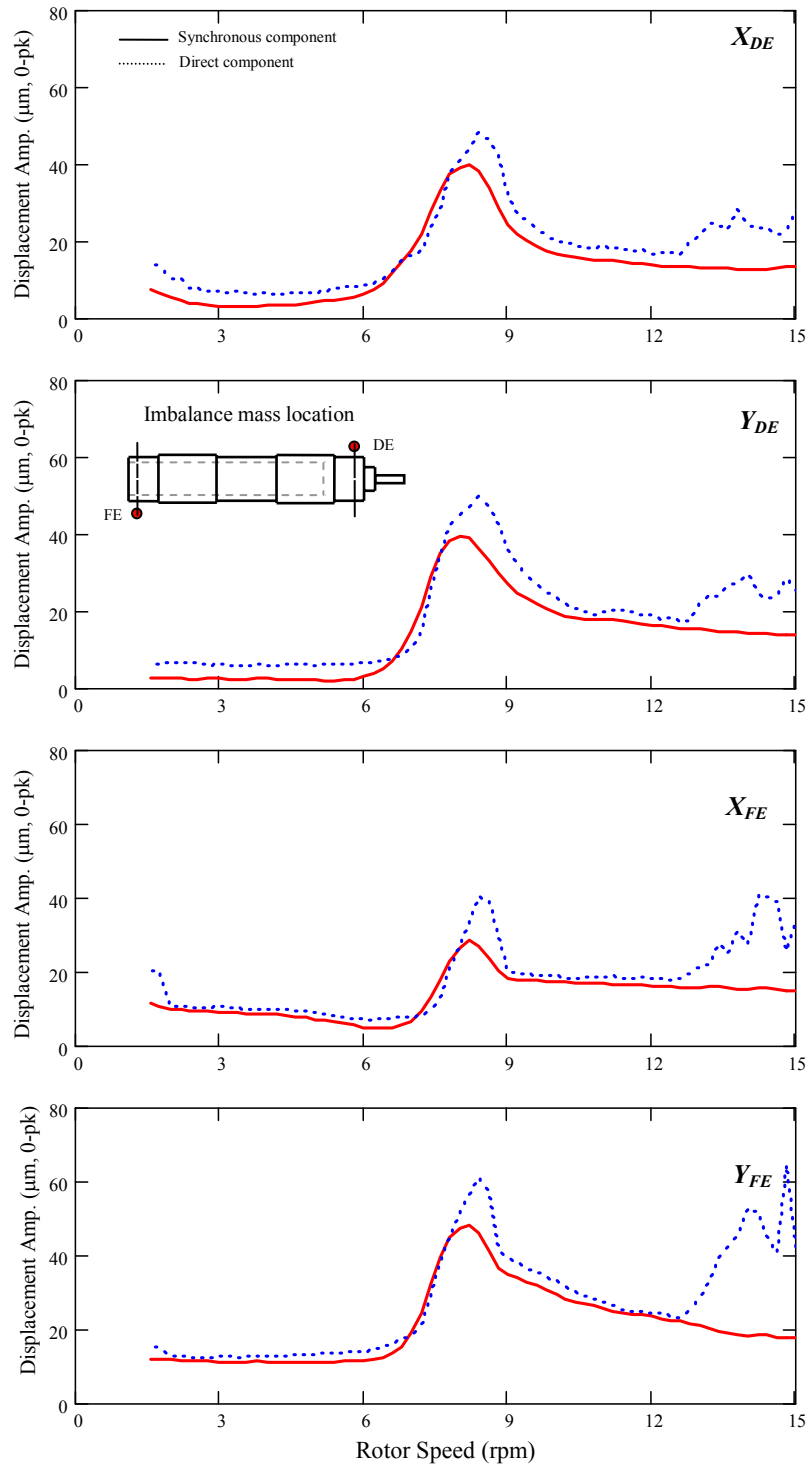## APPENDIX F. SYNCHRONOUS AND DIRECT ROTOR RESPONSES FOR IMBALANCE DISPLACEMENTS A2, B1 AND B3.

Figure F1 Direct and synchronous rotor response for an imbalance u **= 9.5** μm **(in phase, Test A2). Air pressure at 34.4 kPa [5 psig]**
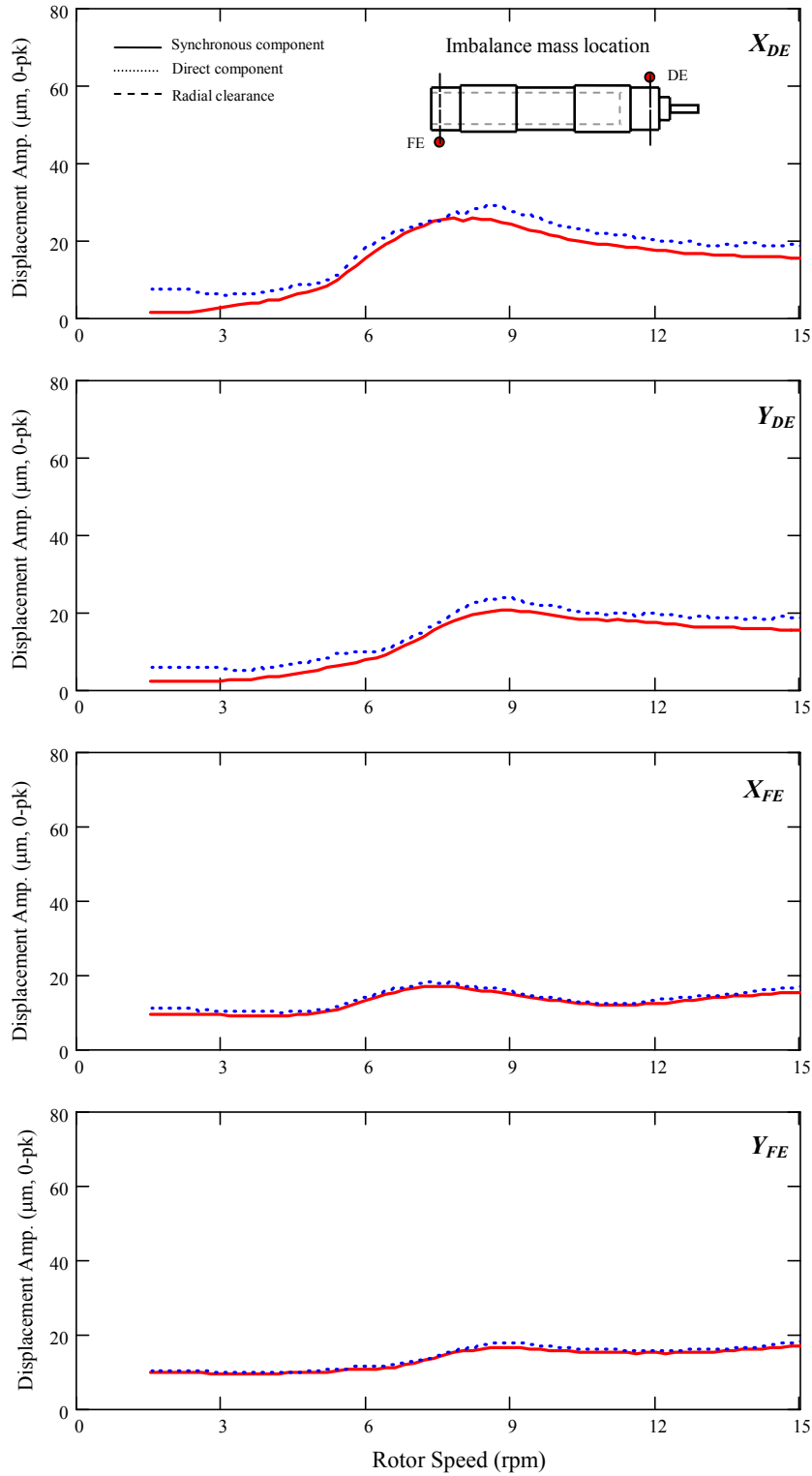
Figure F2 Direct and synchronous rotor response for an imbalance u = 7.4 μm (out of phase, Test B1). Air pressure at 34.4 kPa [5 psig]
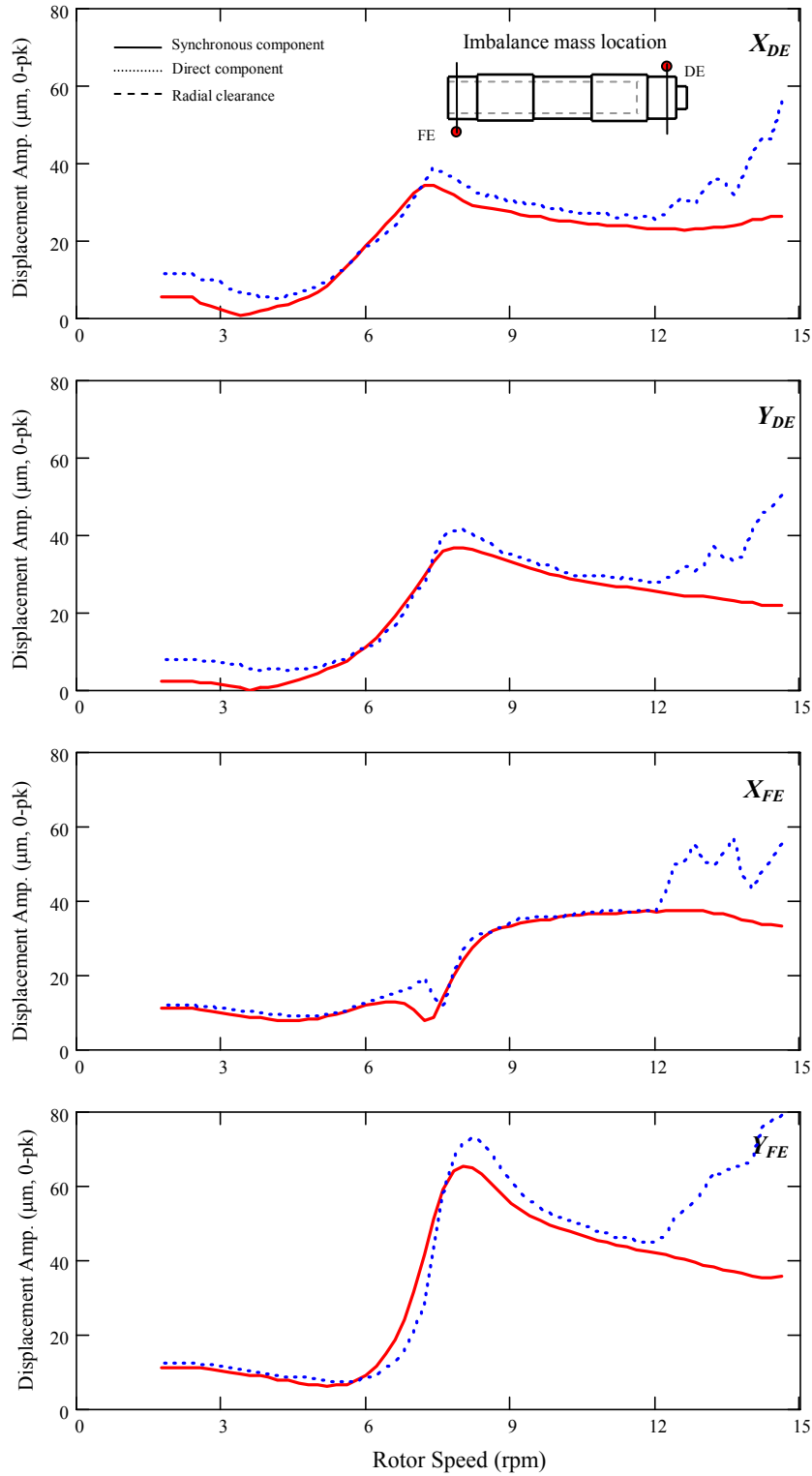
Figure F3 Direct and synchronous rotor response for an imbalance *u* = 10.5 μm (out of phase, Test B3). Air pressure at 34.4 kPa [5 psig]

APPENDIX G. SYNCHRONOUS RESPONSE AND PHASE ANGLE FOR IMBALANCE TESTS *A* IN THE VERTICAL DIRECTION AT THE DRIVE AND FREE ROTOR ENDS.
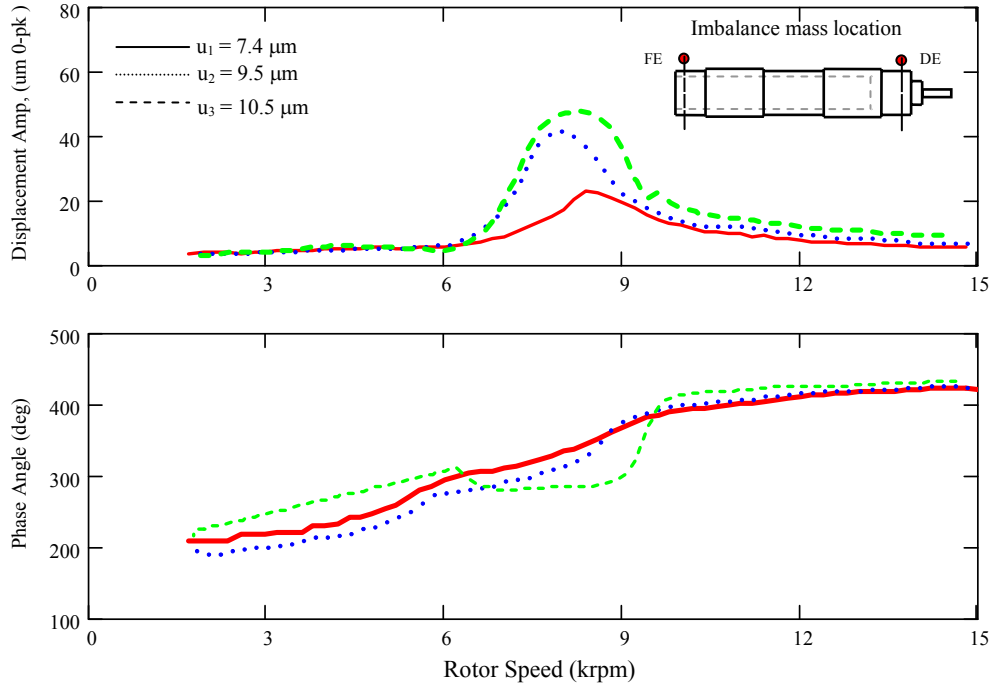

Figure G1 Synchronous rotor response and phase angle for imbalance tests A (in phase). Air pressure at 34.4 kPa [5 psig]. Measurements taken at drive end, vertical direction (Y_{DE})
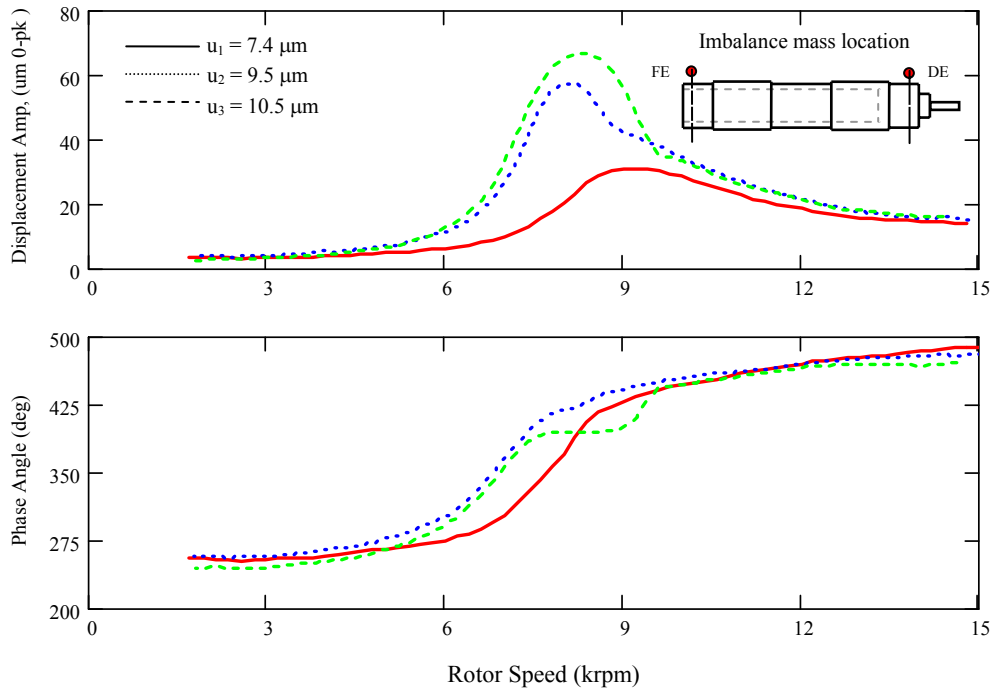
Figure G2 Synchronous rotor response and phase angle for imbalance tests A (in phase). Air pressure at 34.4 kPa [5 psig]. Measurements taken at free end, vertical direction (Y_{FE})

APPENDIX H. SYNCHRONOUS RESPONSE AND PHASE ANGLE FOR IMBALANCE TESTS B IN THE HORIZONTAL DIRECTION AT THE DRIVE AND FREE ROTOR ENDS.
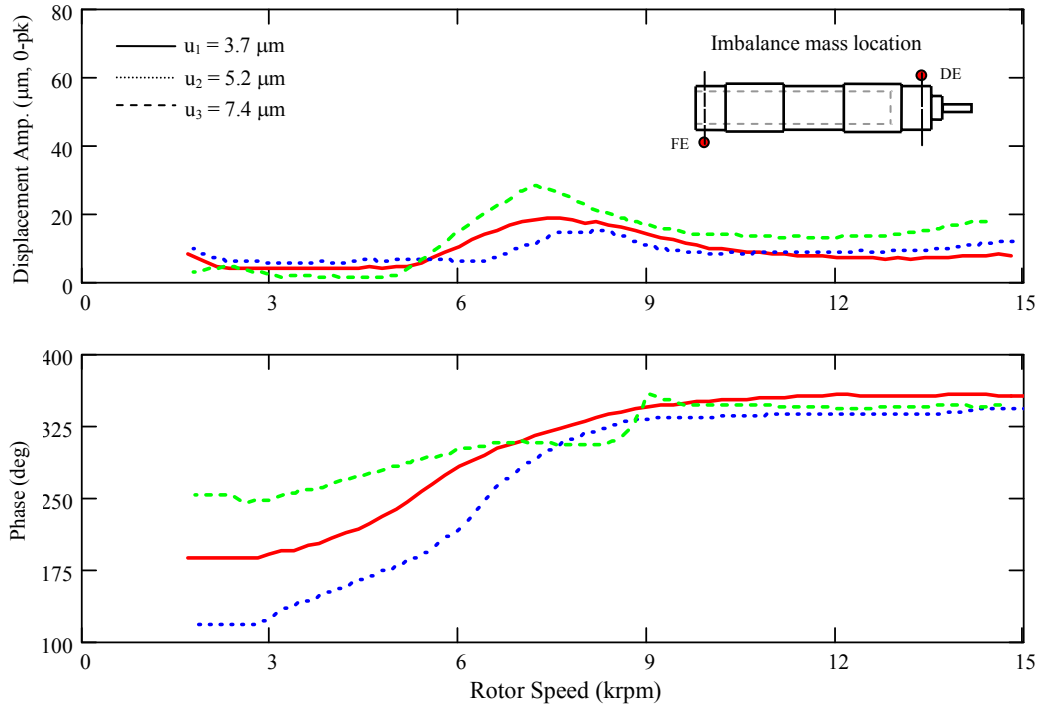

Figure H1 Synchronous rotor response and phase angle for imbalance tests B (out of phase) Air pressure at 34.4 kPa [5 psig]. Measurements taken at drive end horizontal direction (X_{DE})
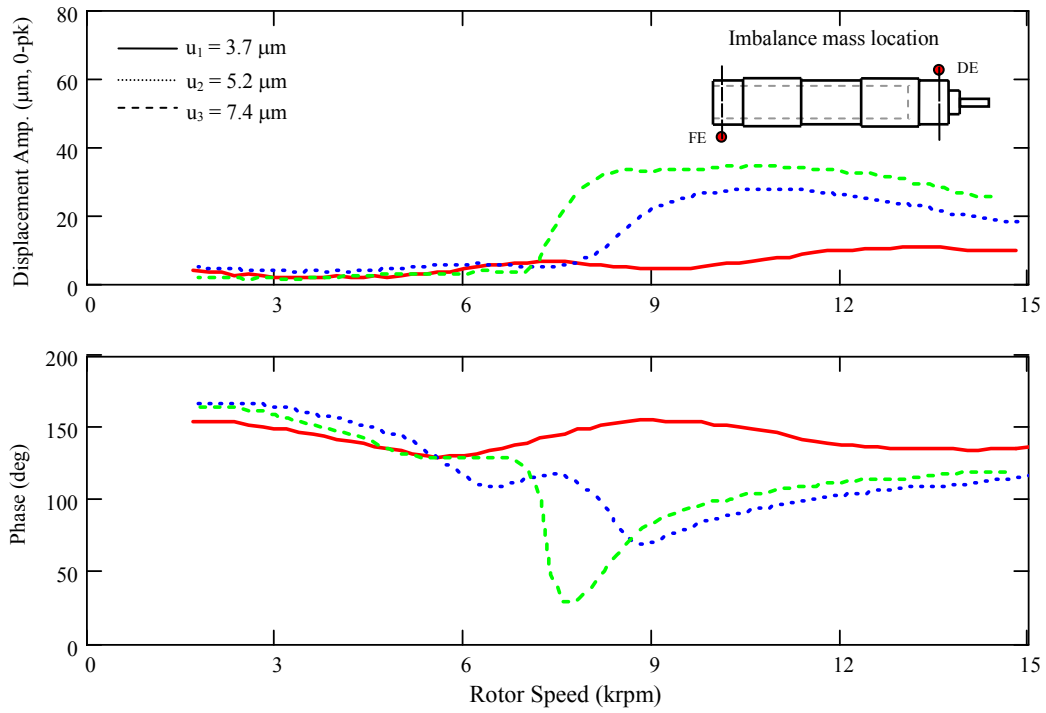
Figure H2 Synchronous rotor response and phase angle for imbalance tests B (out of phase). Air pressure at 34.4 kPa [5 psig]. Measurements taken at free end horizontal direction (X_{FE})